NASA Contractor Report 178296

ICASE REPORT NO. 87-29

ICASE

ARTIFICIAL DISSIPATION AND CENTRAL DIFFERENCE SCHEMES
FOR THE EULER AND NAVIER-STOKES EQUATIONS

R. C. Swanson

Eli Turkel

Contract No. NAS1-18107

April 1987

INSTITUTE FOR COMPUTER APPLICATIONS IN SCIENCE AND ENGINEERING
NASA Langley Research Center, Hampton, Virginia 23665

Operated by the Universities Space Research Association

National Aeronautics and
Space Administration

Langley Research Center
Hampton, Virginia 23665

ARTIFICIAL DISSIPATION AND CENTRAL DIFFERENCE SCHEMES FOR THE EULER AND NAVIER-STOKES EQUATIONS

R. C. Swanson*
NASA Langley Research Center
Hampton, VA

Eli Turkel**
Tel-Aviv University
Tel-Aviv, Israel

ABSTRACT

An artificial dissipation model, including boundary treatment, that is employed in many central difference schemes for solving the Euler and Navier-Stokes equations is discussed. Modifications of this model such as the eigenvalue scaling suggested by upwind differencing are examined. Multistage time stepping schemes with and without a multigrid method are used to investigate the effects of changes in the dissipation model on accuracy and convergence. Improved accuracy for inviscid and viscous airfoil flows is obtained with the modified eigenvalue scaling. Slower convergence rates are experienced with the multigrid method using such scaling. The rate of convergence is improved by applying a dissipation scaling function that depends on mesh cell aspect ratio.

---

*Research Scientist, Theoretical Aerodynamics Branch, TAD. Member AIAA.

**Professor, School of Mathematical Sciences.

Research for the second author was supported by the National Aeronautics and Space Administration under NASA Contract No. NAS1-18107 while he was in residence at the Insitute for Computer Applications in Science and Engineering (ICASE), NASA Langley Research Center, Hampton, VA 23665.

I. INTRODUCTION

In the past few years, substantial progress has been achieved in the development of efficient numerical schemes for solving the Euler and Navier-Stokes equations[1-6]. Robustness and accuracy of the schemes has also continued to improve. Strong emphasis has been placed on sharp representation of shock waves, which is reflected in the Euler solutions obtained[7-10]. Now, the accuracy of viscous flow calculations (i.e., turbulent flows where there are strong gradients) requires additional attention. For example, nonphysical solutions have been obtained for trailing edge turbulent airfoil flows[11-14]. A major factor contributing to inaccuracies is the artificial dissipation present in the numerical algorithms.

The schemes that are used for solving the Euler and Navier-Stokes equations are based on either central or upwind differencing. Both central and upwind methods include artificial dissipation. A symmetric form[15] for the numerical flux function clearly reveals that upwind schemes involve a matrix dissipation coefficient. This results in a specific scaling (based on characteristic values) of the dissipation of each conservation equation. In the case of central difference schemes, a scalar coefficient is employed for the dissipative flux contribution to the numerical flux. This results in a simpler scheme with a smaller operations count. For either type of differencing, the principal requirements in the design of the dissipative terms are that they must be large enough for a satisfactory convergence rate and yet sufficiently small that accuracy is not compromised.

In this paper, a central differencing algorithm is used to investigate artificial dissipation. There are two fundamental reasons for adding dissipation terms to a central difference method. First, they are included to pro-

vide high frequency damping. It is well-known that central difference schemes experience odd and even point decoupling for both linear and nonlinear problems. These high frequency modes must be damped to achieve satisfactory convergence. In the case of nonlinear problems, high frequency damping is required to remove the energy produced by nonlinear interactions (i.e., consider a Fourier representation of nonlinear convection terms). Without such damping, the unresolvable modes (subgrid frequency components) can appear as errors in the resolvable low frequency components of the discrete solution. Second, artificial dissipation terms are added to eliminate oscillations in the neighborhood of shock waves. Also, from the mathematical theory for hyperbolic systems of inviscid conservation laws[16], the introduction of artificial dissipation is necessary to guarantee a unique weak solution.

It is interesting to note that if sufficient resolution were used to define a shock structure, the solution of the full Navier-Stokes equations would eliminate the need for artificial dissipation at shock waves[17]. However, this would mean that the mesh spacing in the streamwise direction in the vicinity of the shock would have to be orders of magnitude (depending on the Reynolds number) smaller than that which is currently used in aerodynamic computations. Furthermore, solving the complete Navier-Stokes equations rather than a subset such as the thin-layer Navier-Stokes equations (where diffusion terms in the streamwise-like direction are neglected) could require much greater computer time.

In the present work, the artificial dissipation model introduced by Jameson, Schmidt, and Turkel[18] is reviewed. Then, some modifications of this model and boundary treatment of the dissipative terms are discussed. Numerical methods used to solve the Euler and thin-layer Navier-Stokes equations are

briefly described. Next, inviscid, laminar, and turbulent airfoil flows are considered to investigate the effects of certain modifications of the basic dissipation model on efficiency and accuracy. Special emphasis is given to the calculation of accurate viscous flow solutions.

II. BASIC DISSIPATION MODEL

The basic dissipation model considered in this paper was first introduced by Jameson, Schmidt and Turkel[18] in conjunction with Runge-Kutta explicit schemes. It has subsequently been used by many investigators[19-23] in a wide range of applications. Also, it has been applied to ADI implicit schemes[24]. In this section, this model will be briefly reviewed.

Consider the Euler equations in the form

$$W_t + f_x + g_y = 0 \tag{1}$$

where W is the solution vector of conserved variables, and f, g are the inviscid flux vectors. The independent variables are time t and Cartesian coordinates (x,y). Transforming Eq. (1) to arbitrary curvilinear coordinates $\xi = \xi(x,y)$, $\eta = \eta(x,y)$

$$(J \cdot W)_t + F_\xi + G_\eta = 0 \tag{2}$$

where J is the transformation Jacobian and $F = fy_\eta - gx_\eta$, $G = gx_\xi - fy_\xi$. In a cell centered finite-volume method, Eq. (2) is simply integrated over an elemental volume in the discretized computational domain, and J is then the

volume of the cell. Eq. (2) can also be written as

$$W_t + AW_\xi + BW_\eta = 0 \tag{3}$$

where A and B are the flux Jacobian matrices.

A typical step of a Runge-Kutta approximation to Eq. (2) is

$$W^{(k)} = W^{(0)} - \alpha_k J^{-1}\Delta t \left[D_\xi F^{(k-1)} + D_\eta G^{(k-1)} - D\right] \tag{4}$$

where D_ξ, D_η are approximations to the spatial derivatives, and D are artificial dissipation terms, which are usually frozen at the first or second stage. The artificial dissipation employed in Ref. 18 is a blending of second and fourth differences. That is,

$$D = (D_\xi^2 + D_\eta^2 - D_\xi^4 - D_\eta^4)W \tag{5}$$

where

$$D_\xi^2 W = \nabla_\xi(\lambda_{i+1/2,j} \cdot \varepsilon^{(2)}_{i+1/2,j})\Delta_\xi W_{i,j}, \tag{6}$$

$$D_\xi^4 W = \nabla_\xi(\lambda_{i+1/2,j} \cdot \varepsilon^{(4)}_{i+1/2,j})\Delta_\xi\nabla_\xi\Delta_\xi W_{i,j}, \tag{7}$$

and Δ_ξ, ∇_ξ are forward and backward difference operators associated with the ξ direction. The variable scaling factor

$$\lambda_{i+1/2,j} = 1/2[(\lambda_\xi)_{i,j} + (\lambda_\xi)_{i+1,j} + (\lambda_\eta)_{i,j} + (\lambda_\eta)_{i+1,j}] \tag{8}$$

where λ_ξ is the largest eigenvalue of the matrix A, and λ_η is the

largest eigenvalue of the matrix B. The coefficients $\varepsilon^{(2)}$ and $\varepsilon^{(4)}$ are adapted to the flow and are defined as follows:

$$\varepsilon^{(2)}_{i+1/2,j} = K^{(2)} \max (\nu_{i,j}, \nu_{i+1,j}), \tag{9}$$

$$\nu_{i,j} = \left| \frac{P_{i+1,j} - 2P_{i,j} + P_{i-1,j}}{P_{i+1,j} + 2P_{i,j} + P_{i-1,j}} \right|, \tag{10}$$

$$\varepsilon^{(4)}_{i+1/2,j} = \max \left[0, (K^{(4)} - \varepsilon^{(2)}_{i+1/2,j})\right], \tag{11}$$

where P is the pressure, and typical values of the constants $K^{(2)}$ and $K^{(4)}$ are 1/4 and 1/256, respectively. The operators in Eq. (5) for the η direction are defined in a similar manner.

Before proceeding, some general comments on the form of these terms are appropriate. First, the original use of this artificial dissipation was for the solution of the Euler equations on a grid with an aspect ratio close to one. Second, the scaling factor λ, which is given in Eq. (8), has an isotropic behavior. Such a behavior is generally not satisfactory in viscous flow calculations. Also, the eigenvalues

$$\begin{aligned} \lambda_\xi &= |uy_\eta - vx_\eta| + c\sqrt{y_\eta^2 + x_\eta^2}\,, \\ \lambda_\eta &= |vx_\xi - uy_\xi| + c\sqrt{x_\xi^2 + y_\xi^2}\,, \end{aligned} \tag{12}$$

where u, v are Cartesian velocity components and c is the speed of sound, represent approximations to the flux Jacobian matrices A and B. (See Refs. 15 and 24 for the relationship between central differencing plus artificial

dissipation and upwind differencing.) Finally, in more recent versions of the dissipation model, the maximum in Eq. (9) is taken over more mesh cells than the immediate neighbors. This is beneficial for shock capturing capability.

III. MODIFICATIONS OF BASIC DISSIPATION MODEL

The second difference dissipation term given in Eq. (6) is an approximation to

$$(\Delta\xi)^2 \frac{\partial}{\partial\xi} (\beta^{(2)} \frac{\partial W}{\partial\xi}),$$

where $\beta^{(2)} = \lambda \cdot \varepsilon^{(2)}$. Adding this expression to the right-hand side (RHS) of Eq. (2), multiplying the resulting equation by W, and integrating over the domain (Ω) gives

$$1/2 \frac{\partial}{\partial t} \int\int_{\Omega} W^2 \cdot J d\xi d\eta = \text{flux terms} - \int\int_{\Omega} \beta^{(2)} (\frac{\partial W}{\partial\xi})^2 d\xi d\eta \tag{13}$$

if boundary terms are neglected or if boundary derivatives vanish. For linear problems, the square of the L^2 norm $\int\int_{\Omega} W^2 \cdot J d\xi d\eta$ (which in this case is an energy estimate in the mathematical sense) is a good measure for the stability of the numerical scheme. Equation (13) shows that the second difference dissipation term decreases this L^2 norm and, thus, is strictly dissipative. If the same type of analysis is done for the fourth difference dissipation term of Eq. (7), then

$$1/2\,\frac{\partial}{\partial t}\int\int_{\Omega} W^2 \cdot J\,d\xi\,d\eta = \text{flux terms}$$

$$-\int\int_{\Omega} \beta^{(4)}\left(\frac{\partial^2 W}{\partial \xi^2}\right)^2 d\xi\,d\eta \qquad (14)$$

$$-\int\int_{\Omega} \frac{\partial \beta^{(4)}}{\partial \xi}\left(\frac{\partial W}{\partial \xi}\right)\cdot\frac{\partial^2 W}{\partial \xi^2}\,d\xi\,d\eta .$$

Both a dissipative term and a dispersive term appear on the RHS of Eq. (14). The following term

$$D_\xi^4 W = (\nabla_\xi \Delta_\xi)\,(\lambda_{i,j} \cdot \xi^{(4)}_{i,j}\,\nabla_\xi \Delta_\xi)\,W_{i,j} \qquad (15)$$

is considered as a replacement for the one in Eq. (7). This modified term produces only dissipative terms. Note that λ and $\varepsilon^{(4)}$ are evaluated at nodes rather than at mesh cell boundaries as in Eq. (7).

For Navier-Stokes problems, a fine mesh is required in the direction normal to the body in order to resolve the boundary layer. In the interest of computational efficiency, the mesh spacing in the streamwise direction for high Reynolds number calculations is generally chosen so as to resolve the streamwise inviscid terms only (i.e., thin-layer Navier-Stokes assumption). Then the mesh in the viscous region has a high aspect ratio (with S as arc length $\Delta S_\eta/\Delta S_\xi \ll 1$). To make matters more difficult, the situation can be reversed in the far field of an external flow problem. Thus, depending on the grid generation technique $\Delta S_\eta/\Delta S_\xi = 0(1)$ or even $\Delta S_\eta/\Delta S_\xi \gg 1$ in the far-field region. These large distortions create difficulties both for the convergence and for the accuracy of steady-state computations. These difficulties are compounded for multigrid schemes since high frequency modes are very different in the two coordinate directions.

A number of investigators have suggested that an anisotropic dissipation model is needed for such problems. Therefore, Eq. (8) in the basic dissipation model is replaced by

$$\lambda_{i+1/2,j} = 1/2[(\lambda_\xi)_{i,j} + (\lambda_\xi)_{i+1,j}], \tag{16}$$

and a similar equation is used in the η direction. For a multigrid algorithm, this scaling in the streamwise direction can be too severe. Moreover, the effectiveness of the driving scheme in damping high frequencies in the ξ direction can be significantly diminished, resulting in a much slower convergence rate. In Ref. 25, Martinelli introduces functions of mesh cell aspect ratio and obtains accurate solutions and good convergence rates. For example, one can replace Eq. (16) by

$$\lambda_{i+1/2,j} = 1/2[(\bar{\lambda}_\xi)_{i,j} + (\bar{\lambda}_\xi)_{i+1,j}]$$

where

$$(\bar{\lambda}_\xi)_{i,j} = \phi_{i,j}(r) \cdot (\lambda_\xi)_{i,j},$$

$$\phi_{i,j}(r) = 1 + r_{i,j}^{\alpha} \qquad 0 < \alpha < 1, \tag{17}$$

and $r = \lambda_\eta/\lambda_\xi$. In the normal direction, one defines

$$(\bar{\lambda}_\eta)_{i,j} = \phi_{i,j}(\tfrac{1}{r}) \cdot (\lambda_\eta)_{i,j}.$$

This is only one possible function, and it should not be considered the optimum.

Due to large velocity gradients in turbulent boundary layers, additional scaling of the artificial dissipation is required in the direction normal to a surface boundary. The presence of the physical viscous terms can be exploited to allow the additional dissipation terms in the normal direction to be reduced. In the present work, this is accomplished by multiplying the second and fourth difference dissipation terms by a simple linear function of the local Mach number. That is, the normal scaling factor becomes

$$\lambda^*_{i,j+1/2} = \frac{f(\tilde{M})}{2} \left[(\lambda_\eta)_{i,j} + (\lambda_\eta)_{i,j+1} \right] \tag{18}$$

where $\tilde{M} = M_L/M_\infty$ and M_L is the local Mach number.

IV. BOUNDARY TREATMENT OF DISSIPATION TERMS

In this section, the boundary dissipation operators that are applied in many flow prediction codes based on finite-volume discretization are presented. Then, a local mode analysis is used to examine the relative damping characteristics of some of the difference stencils. The influence of the boundary cell operators on the character of the dissipation matrix for the system of flow difference equations is also discussed.

In a finite-volume method, the first and last cells in each coordinate direction are auxiliary cells where the flow equations are not solved. The solution in these cells is found by a combination of the given physical boundary conditions and numerical boundary conditions (i.e., extrapolation). Hence, there is generally no difficulty in evaluating the second difference dissipation term at the first or last interior cell in a given coordinate

direction. Note that at a solid surface boundary either the surface or entire contribution to the normal-like dissipation of the first interior cell is usually set to zero. In the case of the fourth difference dissipation term, information is required at two neighboring cells on each side of the cell being considered. Therefore, special treatment of this term is needed for the first interior cell at the boundaries of the physical domain. Eriksson and Rizzi[26] and Pulliam[24] suggest choosing a boundary cell difference stencil that results in a nonpositive definite dissipation matrix for the system of difference equations. As will be shown, such a choice results in a numerical scheme that is more dissipative for the long wavelength components of the solution at a boundary than in the interior of the domain. Although this may be acceptable at a far-field boundary of an external flow problem, caution should be exercised in selecting the difference formula at a solid boundary. For example, in Euler calculations a large dissipation in the direction normal to the boundary can generate a thick false entropy layer. Also, as indicated previously, it can alter a viscous flow solution significantly.

At this point some simplifying notation is introduced to identify and subsequently analyze some of the boundary cell treatments that are commonly used for the fourth-difference dissipation. First, let $\overline{D}$, $\overline{E}$, $\overline{F}$, and $\overline{G}$ denote first, second, third, and fourth differences, respectively. Then, for interior cells in a given direction

$$\overline{D}_{\ell+1/2} = W_{\ell+1} - W_{\ell}$$

$$\overline{E}_{\ell} = \overline{D}_{\ell+1/2} - \overline{D}_{\ell-1/2} = W_{\ell+1} - 2W_{\ell} + W_{\ell-1}$$

$$\overline{F}_{\ell+1/2} = \overline{E}_{\ell+1} - \overline{E}_{\ell} = W_{\ell+2} - 3W_{\ell+1} + 3W_{\ell} - W_{\ell-1}$$

$$\overline{G}_{\ell} = \overline{F}_{\ell+1/2} - \overline{F}_{\ell-1/2} = W_{\ell+2} - 4W_{\ell+1} + 6W_{\ell} - 4W_{\ell-1} + W_{\ell-2},$$

where W_{ℓ} is the discrete solution for the ℓ^{th} cell. The dissipation stencils considered for the first interior cell (designated $\ell = 2$) are generated by applying the following (see Fig. (1)):

(A1) $\overline{D}_{1/2} = \overline{D}_{3/2}$ (zeroth order extrapolation) or $\overline{E}_1 = 0$.

(A2) $\overline{D}_{1/2} = 2\overline{D}_{3/2} - \overline{D}_{5/2}$ (first order extrapolation) or $\overline{E}_1 = \overline{E}_2$. .

(A3) $\overline{D}_{1/2} = \overline{D}_{3/2} + \overline{D}_{5/2} - \overline{D}_{7/2}$ or $\overline{E}_1 = \overline{E}_3$.

(A4) $\overline{D}_{1/2} = 3(\overline{D}_{3/2} - \overline{D}_{5/2}) + \overline{D}_{7/2}$ (quadratic interpolation) or $\overline{E}_1 = -\overline{F}_{5/2} + \overline{D}_{5/2} - \overline{D}_{3/2}$. Then, $\overline{G}_2 = 0$.

In the case of a solid surface boundary ($\ell = 3/2$), the normal difference operators that are generally used are constructed by setting the surface dissipative flux $\overline{F}_{3/2}$ to zero and

(B1) $\overline{D}_{3/2} = \overline{D}_{5/2}$ or $\overline{E}_2 = 0$.

(B2) $\overline{D}_{3/2} = 2\overline{D}_{5/2} - \overline{D}_{7/2}$ or $\overline{E}_2 = \overline{E}_3$.

(B3) $\overline{F}_{5/2} = 0$, $\overline{G}_3 = 0$ (numerical dissipation of zero for first two interior cells).

The treatment of (B3) has been applied successfully in both inviscid and viscous multidimensional flow calculations.[11,23]

A local mode analysis can be beneficial in examining the relative damping behavior of boundary cell difference operators. First, for comparison purposes, we characterize the interior fourth difference. Taking the Fourier transform of $\overline{G}_\ell$ we obtain

$$\overline{g}_\ell = 4(\cos\theta - 1)^2$$

where $\overline{g}_\ell$ is the Fourier symbol and θ is the product of a wave number and the mesh spacing. Then,

$$\overline{g}_\ell \sim \theta^4 \quad \text{for small} \quad \theta$$

and

$$\overline{g}_\ell(\pi) = 16.$$

The dissipation of long waves is dictated by the behavior of $\overline{g}_\ell$ at small θ, and the dissipation of short waves is governed by $\overline{g}_\ell(\pi)$. The coefficient $K^{(4)}$ (see Eq. (11)) is chosen so that the highest frequency is highly damped. This is important for multigrid calculations. Near a boundary, the dissipation should behave in a similar manner.

A general form of the difference stencil at $\ell = 2$ and the associated Fourier transform symbol can be written as follows:

$$\overline{G}_\ell = \alpha W_{\ell+2} - \beta W_{\ell+1} + (\beta + \gamma - \alpha) W_\ell - \gamma W_{\ell-1} \qquad \ell = 2$$

and

$$\overline{g}_\ell = [\beta + \gamma - 2\alpha(1 + \cos\theta)](1 - \cos\theta)$$

$$+ i(\gamma - \beta + 2\alpha \cos\theta)\sin\theta,$$

$$\bar{g}_\ell \approx (\beta + \gamma - 4\alpha)\frac{\theta^2}{2} + \alpha\frac{\theta^4}{2}$$

$$+ i(2\alpha - \beta + \gamma)\theta - i\alpha\theta^3 \quad \text{for small} \quad \theta$$

$$\bar{g}_\ell(\pi) = 2(\beta + \gamma).$$

In the case of (A1)

$$\bar{G}_\ell = W_{\ell+2} - 4W_{\ell+1} + 5W_\ell - 2W_{\ell-1} \qquad \ell = 2,$$

$$\bar{g}_\ell = 4(1 - \cos\theta) - 2e^{i\theta}(1 - \cos\theta),$$

$$\bar{g}_\ell \approx \theta^2 - i\theta^3 \qquad \text{for small} \quad \theta,$$

$$\bar{g}_\ell(\pi) = 12.$$

Note that $\bar{g}_\ell$ is not real; and thus, there is both dissipation and dispersion near the boundary. This is the dissipation recommended by Pulliam[24]. It is second order on long waves and fairly dissipative on short waves. The treatment of (A2) gives

$$\bar{G}_\ell = W_{\ell+2} - 3W_{\ell+1} + 3W_\ell - W_{\ell-1} \qquad \ell = 2,$$

$$\bar{g}_\ell = 2(1 - \cos\theta)^2 - 2i\sin\theta(1 - \cos\theta),$$

$$\bar{g}_\ell \approx \frac{\theta^4}{2} - i\theta^3 \qquad \text{for small } \theta,$$

$$\bar{g}_\ell(\pi) = 8.$$

For all waves, the Real $(\bar{g}_\ell)$ is half of the interior value. The dissipation formula for (A3) is simply twice that of (A2). Then, the real part of $\bar{g}_\ell$ for all waves becomes the same as it is in the interior of the domain. In numerical experiments, the boundary cell treatments of (A1) - (A4) resulted in similar solutions and convergence rates.

In Ref. 24, boundary difference stencils are evaluated by computing the eigenvalues of the dissipation matrix for a one-dimensional discrete system that includes a fourth difference dissipation term. Such an evaluation shows that the damping of the highest frequency (as determined by the largest eigenvalue, say λ_{max}) by boundary treatments (A1) - (A3) is nearly the same. Note that as the number of mesh points increases, the eigenvalue λ_{max} is dictated by the interior point stencil (for the interior $\bar{g}_\ell(\pi) = 16$). The principal difference between using (A1) or (A2) - (A3) is indicated by the low frequency behavior of the dissipation matrix (see also $\bar{g}_\ell(\theta)$ for small θ). The matrix associated with (A2) or (A3) has a zero eigenvalue. Therefore, (A2) or (A3) are not recommended since they could lead to undamped modes. According to Refs. 26 and 24 a boundary dissipation formula is chosen so that the dissipation matrix is nonpositive definite (i.e., strictly dissipative). The dissipation treatments resulting from (A1) and (B1) satisfy this requirement. The results of this paper were obtained with (A1) and (B1). Moreover, the boundary treatment and interior representation (Eq. (15)) of the fourth difference dissipation are consistent (i.e., strictly dissipative).

V. NUMERICAL METHODS

The numerical results presented in this paper were computed with multistage time stepping schemes. Details and properties of these schemes have been described previously[11]. In some of the calculations, both four and five stage Runge-Kutta algorithms were used as drivers for a multigrid process. The multigrid technique is based on the work of Jameson.[27] In particular, a Full Approximation Storage (FAS) method[28] and V-type cycle are employed. The grid transfer operators (i.e., restriction and prolongation operators) are the same ones used in the Jameson procedure. Several modifications of the original method have resulted in improved multigrid performance. First, the fourth difference dissipation term is computed with Eq. (15). The normal artificial dissipation near the wake line is treated by continuation rather than applying the same procedure used on the airfoil surface. All boundary information is updated after each stage and on all meshes in the multigrid process. Finally, on each level of refinement of a Full Multigrid (FMG) method, multiple iterations are performed on coarse grids. One iteration is done on the finest mesh, two Runge-Kutta cycles on the next mesh, and three Runge-Kutta cycles on all coarser meshes. In the viscous flow calculations, a convective coarse grid correction scheme is used.[29] Moreover, the viscous terms are evaluated only on the finest grid for a given level of refinement. For further discussion of the multigrid algorithm, see Ref. 30.

VI. RESULTS AND DISCUSSION

Adequate consideration must be given to convergence as well as accuracy in designing an artificial dissipation model. This is especially true for a

multigrid technique. For example, good high frequency damping of the basic solver is the crucial requirement for constructing an efficient multigrid process. In the first part of this section, the effects of scaling of the numerical dissipation are investigated by considering multigrid calculations for inviscid and laminar flow over an airfoil. The last part deals with transonic turbulent airfoil flow, and in particular, the trailing edge flow. To facilitate the discussion of the numerical results, the following designations are made to indicate the form of the artificial dissipation model used:

1) Basic or original (see Section II)
2) Modified (Eq. (16)) - This refers to scaling with individual eigenvalues.
3) Modified (Eq. (17)) - Individual eigenvalues are multiplied by a function of cell aspect ratio.

For each model, Eq. (15) is used for the fourth difference dissipation term. Finally, wherever a convergence history is presented, it shows the variation of the logarithm of the root mean square of the residual of the continuity equation with iteration. For the multigrid computations, an iteration corresponds to a multigrid cycle.

Transonic Inviscid Flow

Several calculations were performed for an NACA 0012 airfoil at Mach 0.8 and an angle of attack of 1.25^{o}. A C-type mesh with 256 cells around the airfoil (193 points on the airfoil) and 32 cells normal to the airfoil was used. The outer boundary was placed 12 chords away from the airfoil; a far

field vortex boundary condition[31] was applied. The computed surface pressure distributions and convergence histories using the basic and modified (Eq. (16)) artificial dissipation models are displayed in Figs. 2 and 3, respectively. The predicted shocks on the upper and lower surfaces of the airfoil are stronger as a result of reducing the numerical dissipation. However, the mean convergence rate with the multigrid method deteriorates substantially. It is .876 with the original model and .960 with the modified (Eq. (16)) model. If the modification of Eq. (17) is applied, the calculated pressure distribution (Fig. 4a) is very close to that given in Fig. 3. Furthermore, the mean convergence rate of the computation is improved significantly (a value of .890 for 100 cycles). It should be emphasized that the function employed in Eq. (17) for scaling the artificial dissipation is by no means optimum. The lift and drag coefficients for these cases and those predicted with the high density mesh calculations of Ref. 7 are given in Table I.

Table I

Lift and drag coefficients for NACA 0012 airfoil, $M_\infty = .8$, $\alpha = 1.25^\circ$

Case	C_L	C_D
Basic dissipation model	.3330	.0220
Modified (Eq. 16)) dissipation model	.3667	.0235
Modified (Eq. 17)) dissipation model	.3567	.0234
Ref. 7 - 561 x 65 C-type mesh	.3618	.0236

Subsonic Laminar Flow

Numerical solutions were obtained for laminar flow past an NACA 0012 airfoil. The Mach number was 0.5, the Reynolds number was 5000, and the angle of attack was zero degrees. A C-type mesh with 256 x 64 cells (129 points on the airfoil) was employed in the calculations. The normal mesh spacing at the surface was about 6×10^{-4} chords, and the trailing edge streamwise spacing was 5×10^{-3} chords. In Figs. 5a and 5b, the pressure and skin-friction distributions computed using the original dissipation model are shown. The absence of any pressure recovery at the trailing edge indicates the presence of strong viscous effects. Moreover, as denoted in Fig. 5b, the flow separates at the .811 chord location. There is a sudden change in the skin friction at the trailing edge. At least in part, this is a consequence of the artificial dissipation model. The convergence history for this case is presented in Fig. 5c. In 300 multigrid cycles with the finest grid (requiring less than 3 minutes on the CRAY II computer), the mean rate of convergence is .923.

The surface skin-friction distribution calculated using the modified (Eq. (16)) model is displayed in Fig. 6a. Now, there is a significantly smaller decrease in the skin friction at the airfoil trailing edge. In the case of the modified (Eq. (17)) model, some additional scaling (with a simple second degree polynomial) in the streamwise direction in the immediate vicinity of the trailing edge was required to obtain essentially the same skin-friction solution and a good convergence rate. Figure 6b shows the convergence histories for these cases. The mean rates of convergence using the modified models based on Eqs. (16) and (17) are .947 and .932, respectively.

For all these laminar flow results the second difference dissipation terms are set to zero. In the shear layers, the normal physical viscous terms generally dominate (are an order of magnitude or more larger than) the numerical dissipation terms. However, even with the modified (Eq. (16)) model, the streamwise artificial dissipation terms are not dominated by the normal physical ones for a few cells surrounding a trailing edge cell. For this laminar case, the streamwise diffusion terms, which were neglected by the thin-layer approximation, may be of sufficient importance to allow domination of the total physical viscous effects over the artificial ones at the trailing edge.

The streamlines of the recirculation zone for the modified (Eq. (16)) dissipation model solution are presented in Fig. 7. The longitudinal and lateral extents of this thin bubble are very close to those predicted with the other models. Figure 8 shows a velocity vector plot for this laminar flow problem.

Transonic Turbulent Flow

Nonphysical solutions for turbulent flow in the trailing edge region of an airfoil have been observed by many investigators. The basic factors that determine the accuracy of the trailing edge solution are as follows:

1) Mesh (resolution and orientation),
2) artificial dissipation,
3) turbulence modelling.

In Ref. 33, Haase indicates that the principal reason for inaccurate results is the nonalignment of the trailing-edge mesh line and streamline. Based on the present work and Ref. 2, this is not considered to be the main cause of inaccuracy. That is, qualitatively correct physical behavior can be obtained, even if the trailing-edge mesh line bisects the trailing-edge angle, as long as the artificial dissipation is sufficiently small.

The impact of the artificial dissipation terms is revealed in results for transonic flow over an RAE 2822 airfoil. In this standard test case,[33] the free-stream Mach number is 0.73, the Reynolds number is 6.5×10^6, and the angle of attack corrected for wind-tunnel wall effects is 2.79 degrees. The first set of results was computed with the basic artificial dissipation model and a C-type mesh having 264×100 cells. A view of the mesh and a blowup of the trailing-edge region is shown in Fig. 9. The mesh spacing in the normal direction at the surface is such that the first mesh point is inside the laminar sublayer. The spacing in the x direction at the trailing edge ($\Delta x_{t.e.}$) is 0.0147 chords. Figures 10a and 10b compare the pressure and upper surface skin-friction distributions with experimental data. Even though there is an adverse pressure gradient on the upper surface near the trailing edge, the skin friction there exhibits a substantial rise, which is not physically correct.

The next set of results was obtained with the basic dissipation model and a finer trailing-edge mesh. The mesh for this case is presented in Fig. 11. The spacing $\Delta x_{t.e.}$ is 0.005 chords. This represents a reduction of almost a factor of three. At the shock wave, the spacing is more than twice that for the previous results. In Figs. 12a and 12b, the pressure and skin-friction variations are displayed. There is still a strong skin friction rise at the airfoil trailing edge.

The final group of results was calculated using the modified (Eq. (16)) dissipation model and the mesh in Fig. 11. They are shown in Figs. 13a - 13d. The predicted pressures are in good agreement with experimental data, even with the coarse grid spacing in the vicinity of the shock. As indicated in Fig. 13b, there are two separated flow regions on the airfoil. A very small shock induced separation bubble occurs at about 56% chord. The trailing edge separation on the upper surface of the airfoil occurs approximately at 95% chord. The behavior of the flow in the vicinity of the trailing edge is clearly visible in Fig. 13c. Figure 13d presents the residual and lift histories for the calculation. A multigrid procedure was not employed. Finally, in Table II the predicted lift, drag, and pitching moment coefficients are compared with those of experiment and Ref. 3.

TABLE II

Lift, drag, and pitching moment coefficients for RAE 2822 airfoil,

$M_\infty = .73$, $Re_\infty = 6.5 \times 10^6$, $\alpha = 2.79^\circ$

	C_L	C_{D_p}	C_{D_f}	C_D	C_M
Experiment (Ref. 33)	.803	-	-	.0168	-.099
Present (256 x 64 C-type mesh)	.829	.0124	.0051	.0175	-.093
Pulliam (Ref. 3, 248 x 51 O-type mesh)	.824	.0128	.0050	.0178	-.092

C_{D_p} - pressure drag coefficient

C_{D_f} - friction drag coefficient

CONCLUDING REMARKS

Improved accuracy of numerical flow solutions has been achieved by modifying a standard artificial dissipation model for central differencing schemes. With the eigenvalue scaling suggested by upwind differencing, the artificial dissipation in the streamwise flow direction has been reduced. This has resulted in a better representation of inviscid transonic flows on a given mesh. In addition, physically correct viscous solutions for the trailing edge of an airfoil flow have been obtained. However, the modified eigenvalue scaling of the dissipation has resulted in slower convergence rates for a multigrid method driven by a multistage time stepping scheme. Improvements in accuracy and multigrid convergence rates have been shown possible by modifying the scaling with a function that depends on mesh cell aspect ratio.

REFERENCES

[1]Jameson, A. and Baker, T. J., "Multigrid Solution of the Euler Equations for Aircraft Configurations," AIAA Paper 84-0093, January 1984.

[2]Martinelli, L., Jameson, A., and Grasso, F., "A Multigrid Method for the Navier-Stokes Equations," AIAA Paper 86-0208, January 1986.

[3]Pulliam, T. H. and Steger, J. L., "Recent Improvements in Efficiency, Accuracy, and Convergence for Implicit Approximate Factorization Algorithms," AIAA Paper 85-0360, January 1985.

[4]Anderson, W. K., Thomas, J. L., and Whitfield, D. L., "Multigrid Acceleration of the Flux Split Euler Equations," AIAA Paper 86-0274, January 1986.

[5]Thomas, J. L., Taylor, S. L., and Anderson, W. K., "Navier-Stokes Computations of Vortical Flows Over Low Aspect Ratio Wings," AIAA Paper 87-0207, January 1987.

[6]Obayashi, S., Matsushima, K., Fujii, K., and Kuwaharo, K., "Improvements in Efficiency and Reliability for Navier-Stokes Computations Using the LU-ADI Factorization Algorithm," AIAA Paper 86-0338, January 1986.

[7]Pulliam, T. H. and Barton, J. T., "Euler Computations of AGARD Working Group 07 Airfoil Test Cases," AIAA Paper 85-0018, January 1985.

[8]Anderson, W. K., Thomas, J. L., and van Leer, B., "A Comparison of Finite-Volume Flux Vector Splittings for the Euler Equations," AIAA J., Vol. 24, No. 9, September 1986, pp. 1453-1460.

[9]Yee, H. C. and Harten, A., "Implicit TVD Schemes for Hyperbolic Conservations Laws in Curvilinear Coordinates," AIAA Paper 85-1513, Proc. AIAA 7th Computational Fluid Dynamics Conference, Cincinnatti, Ohio, July 1985.

[10]Chakravarthy, S. R., "Development of Upwind Schemes for the Euler Equations," NASA CR-4043, January 1987.

[11]Swanson, R. C. and Turkel, E., "A Multistage Time-Stepping Scheme for the Navier-Stokes Equations," AIAA Paper 85-0035, January 1985.

[12]Coakley, T. J., "Turbulence Modelling Methods for the Compressible Navier-Stokes Equations," AIAA Paper 83-1693, July 1983.

[13]Maksymink, C. M. and Pulliam, T. H., "Viscous Transonic Airfoil Workshop Results Using ARC2D," AIAA Paper 87-0415, January 1987.

[14]Rumsey, C. L., Taylor, S. L., Thomas, J. L., and Anderson, W. K., "Application of an Upwind Navier-Stokes Code to Two-Dimensional Transonic Airfoil Flow," AIAA Paper 87-0413, January 1987.

[15]van Leer, B., "Upwind-Difference Methods for Aerodynamic Problems Governed by the Euler Equations," Lectures in Applied Mathematics, Vol. 22, 1985, pp. 327-336.

[16]Lax, P. D., "Hyperbolic Systems of Conservation Laws and the Mathematical Theory of Shock Waves," SIAM Region. Ser. Appl. Math. Vol. II, SIAM, Philadelphia, Pennsylvania, 1973.

[17]Macaraeg, M. G. and Streett, C. L., "A Spectral Multi-Domain Technique with Application to Generalized Curvilinear Coordinates," NASA TM-87701, March 1986.

[18]Jameson, A., Schmidt, W., and Turkel, E., "Numerical Solutions of the Euler Equations by Finite Volume Methods Using Runge-Kutta Time-Stepping Schemes," AIAA Paper 81-1259, June 1981.

[19]Deese, J. E. and Agarwall, R. K., "Calculations of Axisymmetric Inlet Flowfield Using the Euler Equations," AIAA Paper 83-1853, July 1983.

[20]Jameson, A. and Baker, T. J., "Solution of the Euler Equations for Complex Configurations," AIAA Paper 83-1929, Proc. AIAA 6th Fluid Dynamics Conf., Danvers, Massachusetts, July 1983.

[21]Subramanian, S. V. and Bozzola, R., "Application of Runge-Kutta Time Marching Scheme for the Computation of Transonic Flows in Turbomachines," AIAA Paper 85-1332, July 1985.

[22]Davis, R., Ni, R. H., and Carter, J. E., "Cascade Viscous Flow Analysis Using the Navier-Stokes Equations," AIAA Paper 86-0033, January 1986.

[23]Vatsa, V. N., "Accurate Solutions for Transonic Viscous Flow Over Finite Wings," AIAA Paper 86-1052, May 1986.

[24]Pulliam, T. H., "Artificial Dissipation Models for the Euler Equations," AIAA Paper 85-0438, January 1985.

[25]Martinelli, L., "Calculation of Viscous Flows with Multigrid Methods," Ph.D. Dissertion, MAE Department, Princeton University, to be published.

[26]Eriksson, L. E. and Rizzi, A., "Analysis by Computer of the Convergence to Steady State of Discrete Approximations to the Euler Equations," AIAA Paper 83-1951, Proc. AIAA 6th Computational Fluid Dynamics Meetings, Danvers, Massachusetts, July 1983.

[27]Jameson, A., "Transonic Flow Calculations," MAE Report #1651, Princeton University, July 1983.

[28]Brandt, A., "Multi-Level Adaptive Solutions to Boundary-Value Problems," Math. Comp., Vol. 31, No. 138, April 1977, pp. 333-390.

[29]Johnson, G. M., "Convergence Acceleration of Viscous Flow Computations," NASA TM-83039, October 1982.

[30]Chima, R. V. and Turkel, E., "Comparison of Three Explicit Multigrid Methods for the Euler and Navier-Stokes Equations," AIAA Paper 87-0602, January 1987.

[31]Thomas, J. L. and Salas, M. D., "Far-Field Boundary Conditions for Transonic Lifting Solutions to the Euler Equations," AIAA Paper 85-0020, January 1985.

[32]Haase, W., "Influence of Trailing-Edge Meshes on Skin Friction in Navier-Stokes Calculations," AIAA J., Vol. 24, No. 9, September 1986, pp. 1557-1559.

[33]Cook, P. H., McDonald, M. A., and Firmin, M. C. P., "AEROFOIL RAE 2822 Pressure Distributions, and Boundary Layer and Wake Measurements," AGARD Advisory Report No. 138, May 1979.

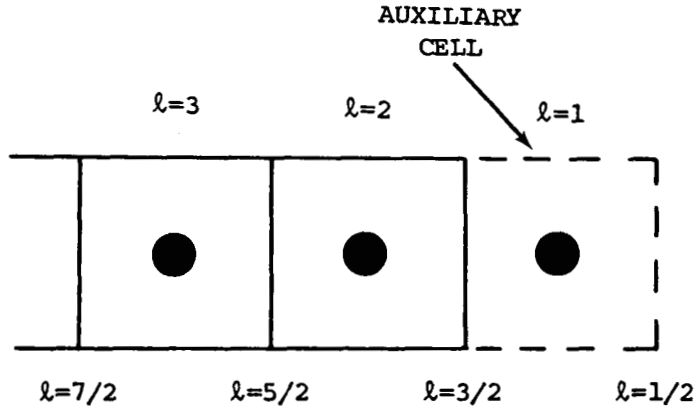

Figure 1. Designation of mesh lines and solution points for boundary cell treatment of artificial dissipation.

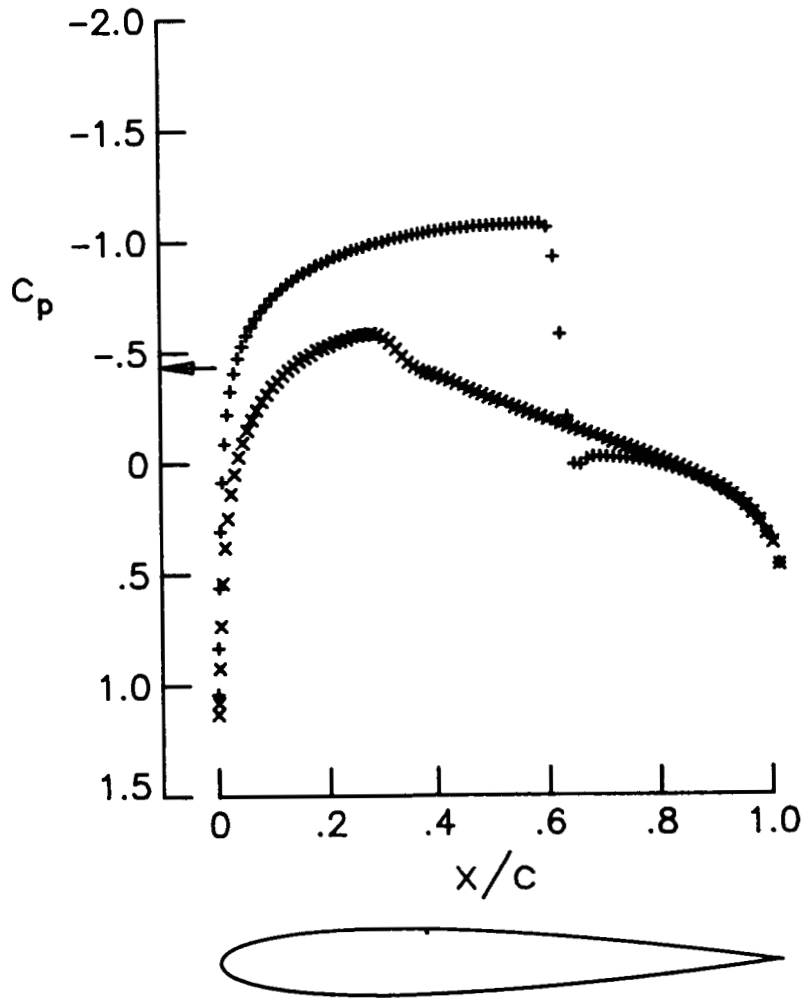

(a) Pressure distribution.

Figure 2. Calculation of inviscid flow over NACA 0012 airfoil using basic artificial dissipation model ($M_\infty = 0.8$, $\alpha = 1.25^o$).

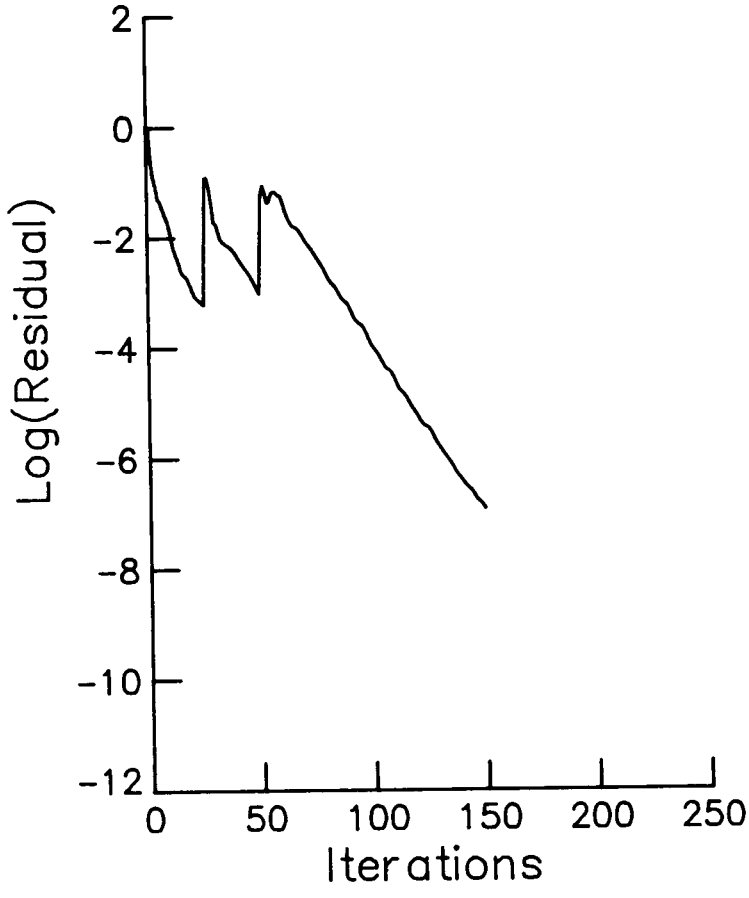

(b) Convergence history.

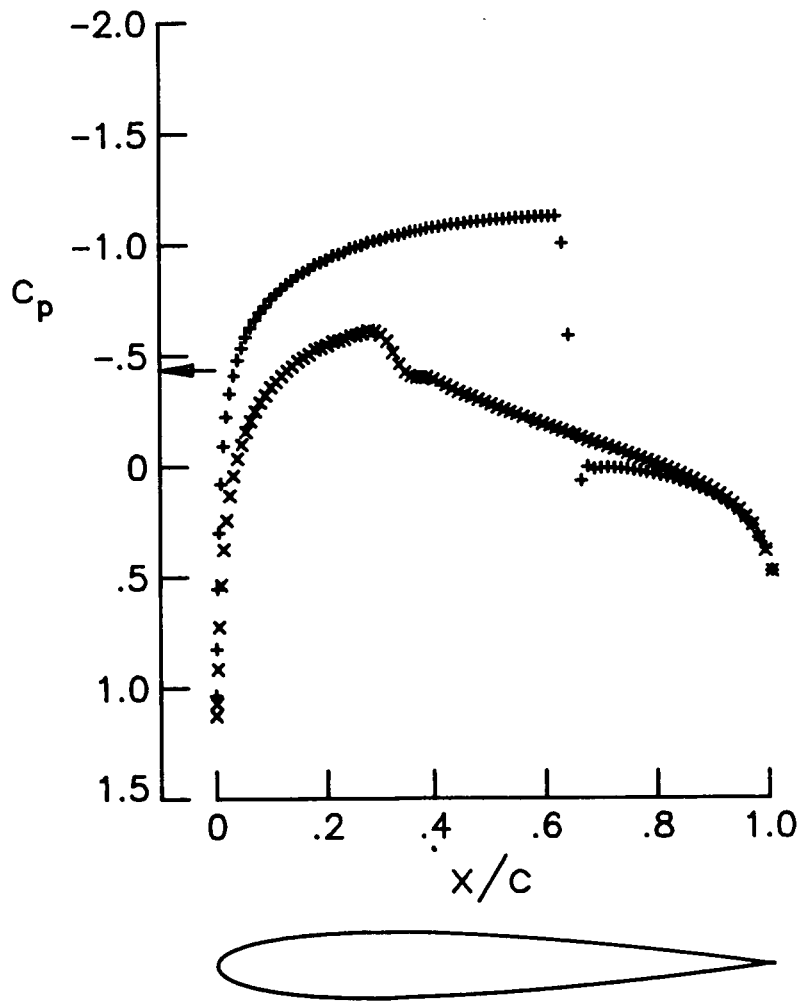

(a) Pressure distribution.

Figure 3. Calculation of inviscid flow over NACA 0012 airfoil using modified (Eq. (16)) artificial dissipation model ($M_\infty = 0.8$, $\alpha = 1.25$).

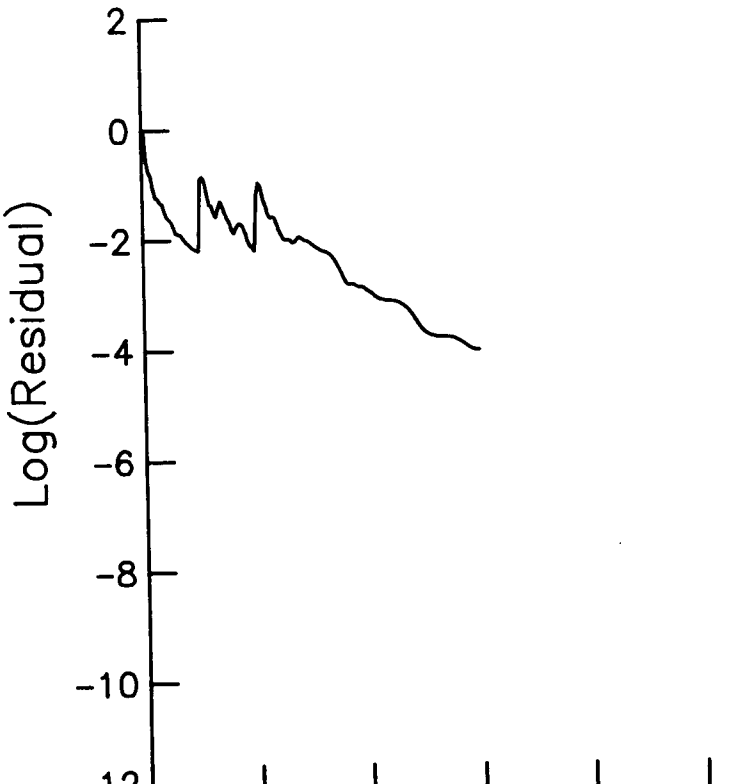

(b) Convergence history.

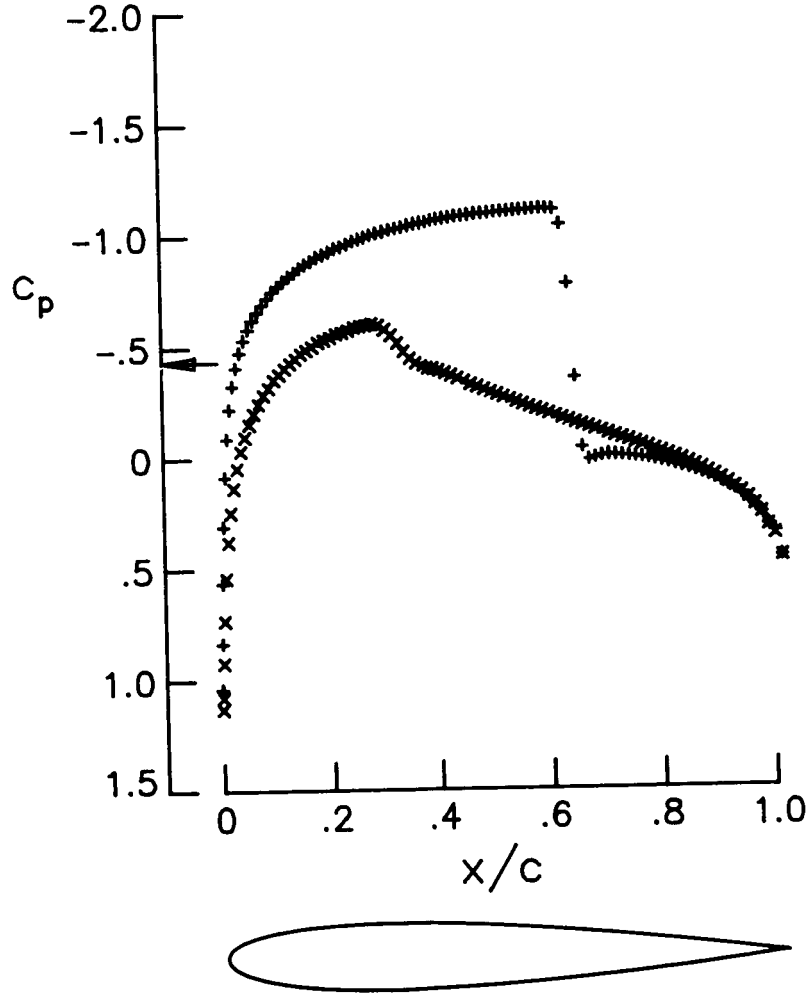

(a) Pressure distribution.

Figure 4. Calculation of inviscid flow over NACA 0012 airfoil using modified (Eq. (17)) artificial dissipation model ($M_\infty = 0.8$, $\alpha = 1.25^o$).

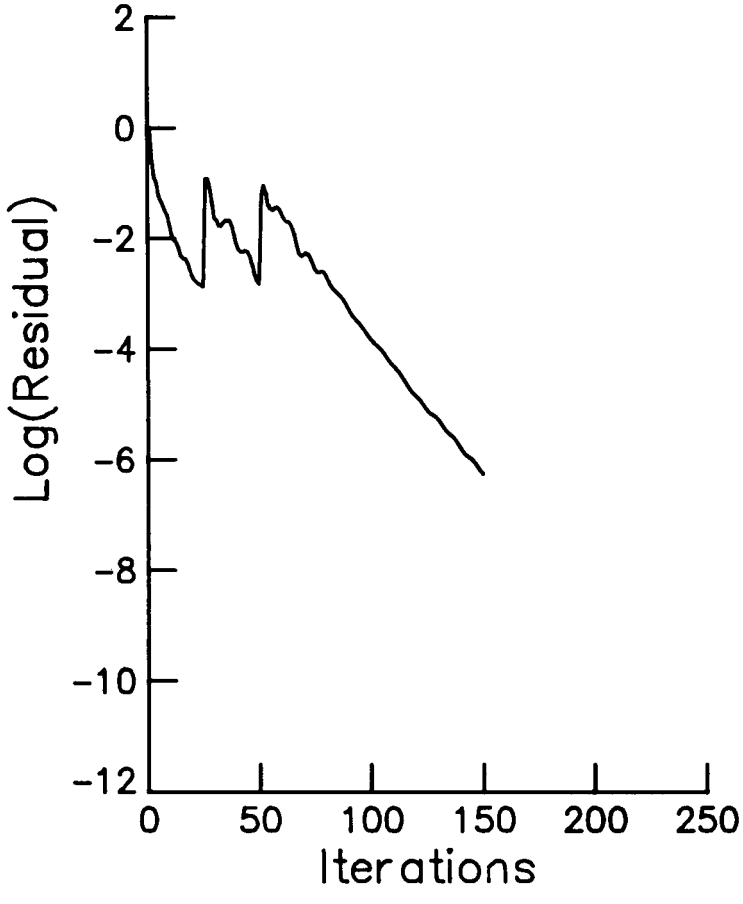

(b) Convergence history.

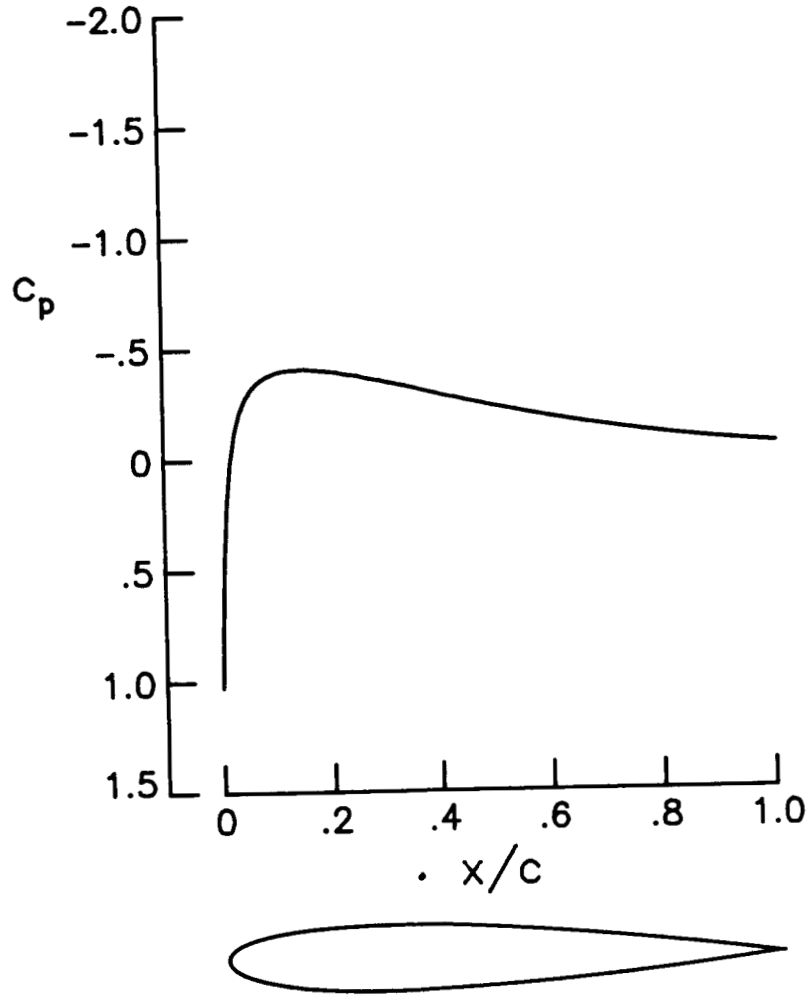

(a) Pressure distribution.

Figure 5. Calculation of laminar flow over NACA 0012 airfoil using basic artificial dissipation model ($M_\infty = 0.8$, $Re_\infty = 5000$, $\alpha = 0^o$).

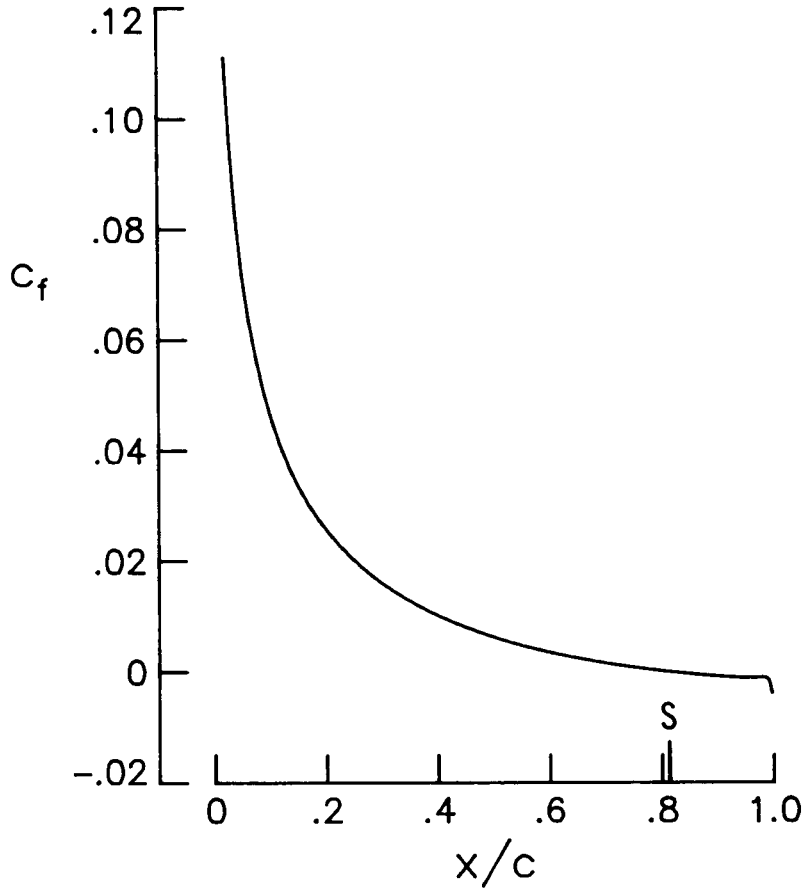

(b) Skin-friction distribution.

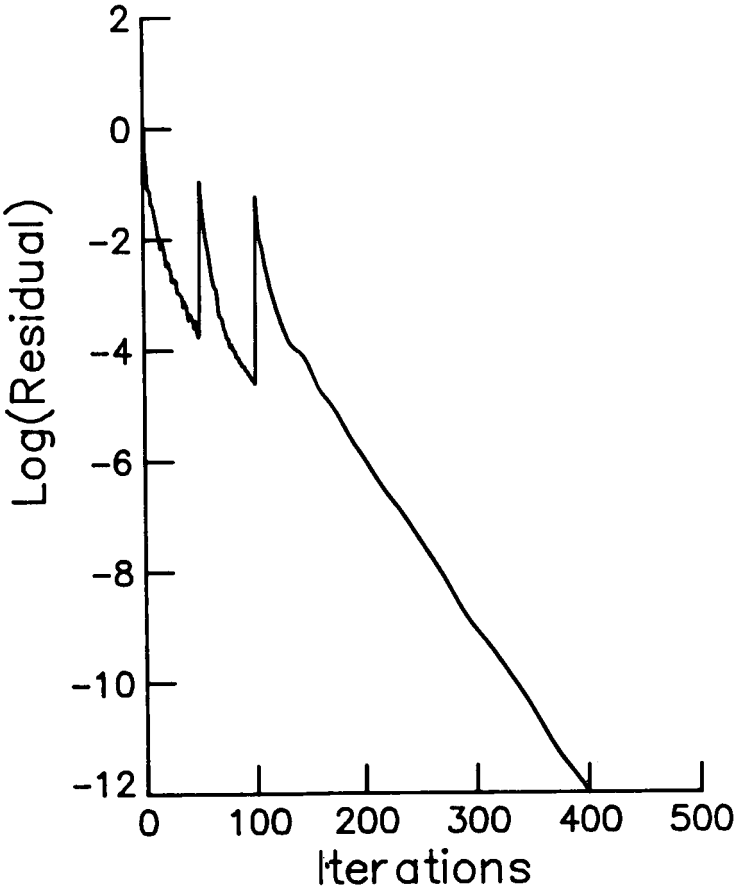

(c) Convergence history.

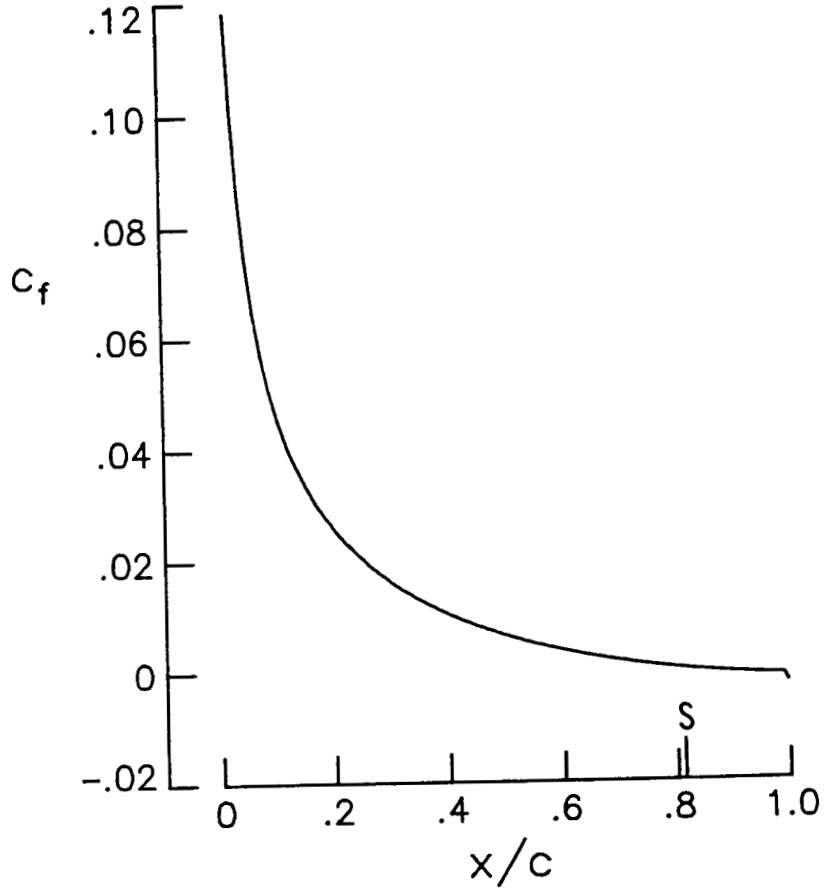

(a) Skin-friction distribution.

Figure 6. Calculations of laminar flow over NACA 0012 airfoil using modified artificial dissipation models ($M_\infty = 0.5$, $Re_\infty = 5000$, $\alpha = 0^\circ$).

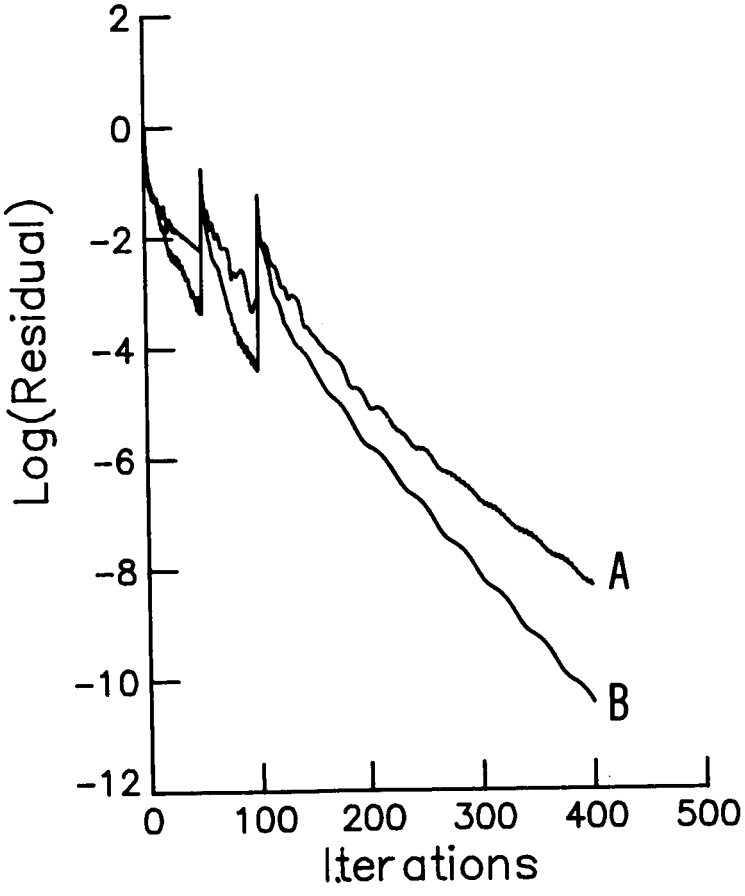

(b) Convergence histories.
A - Modified (Eq. (16)) model
B - Modified (Eq. (17)) model

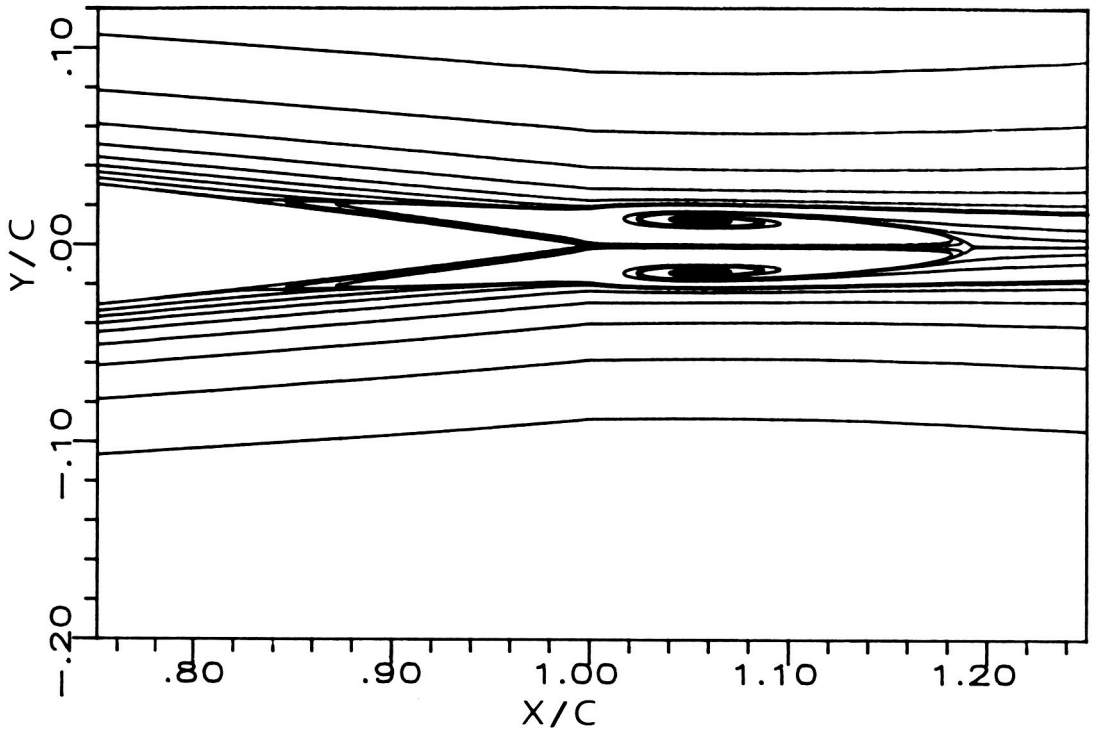

Figure 7. Particle pathlines for laminar flow over NACA 0012 airfoil ($M_\infty = 0.5$, $Re_\infty = 5000$, $\alpha = 0^o$).

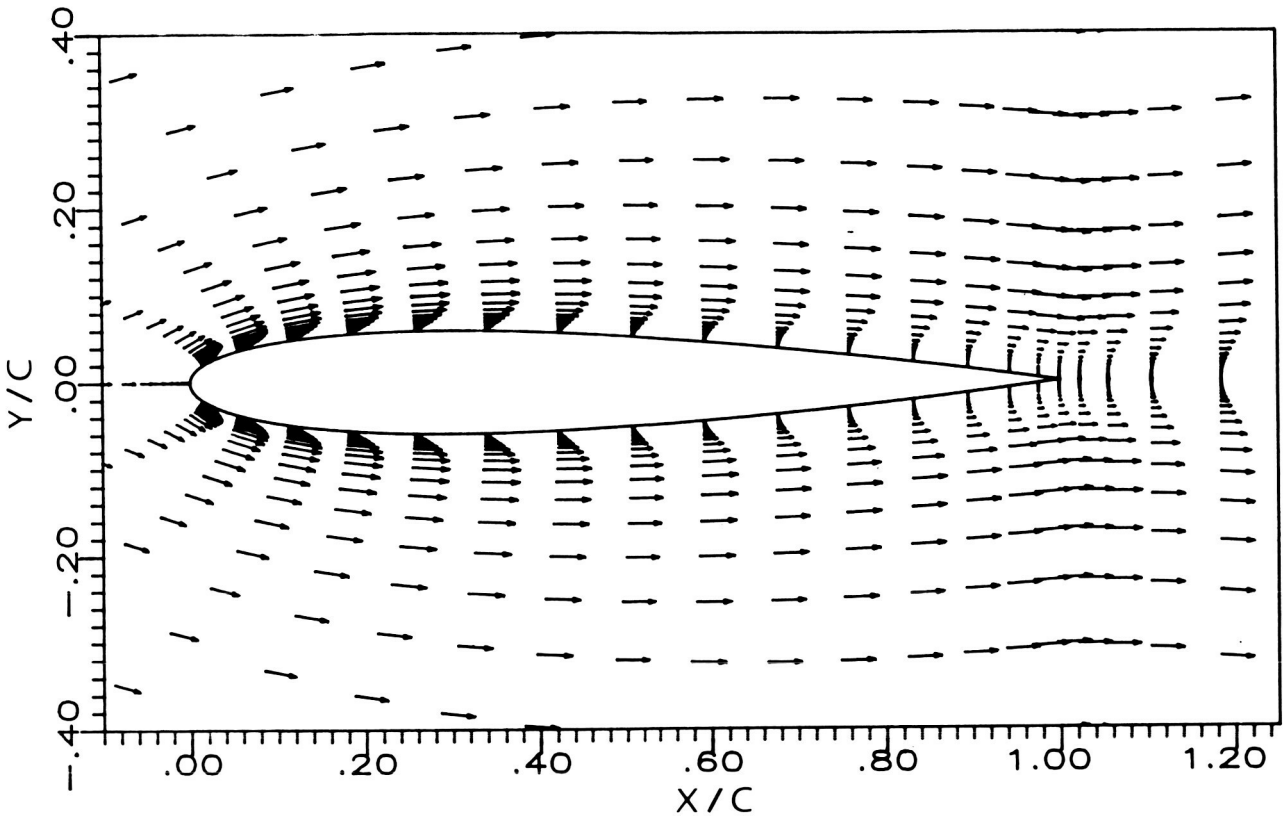

Figure 8. Velocity vectors for laminar flow over NACA 0012 airfoil ($M_\infty = 0.5$, $Re_\infty = 5000$, $\alpha = 0^o$).

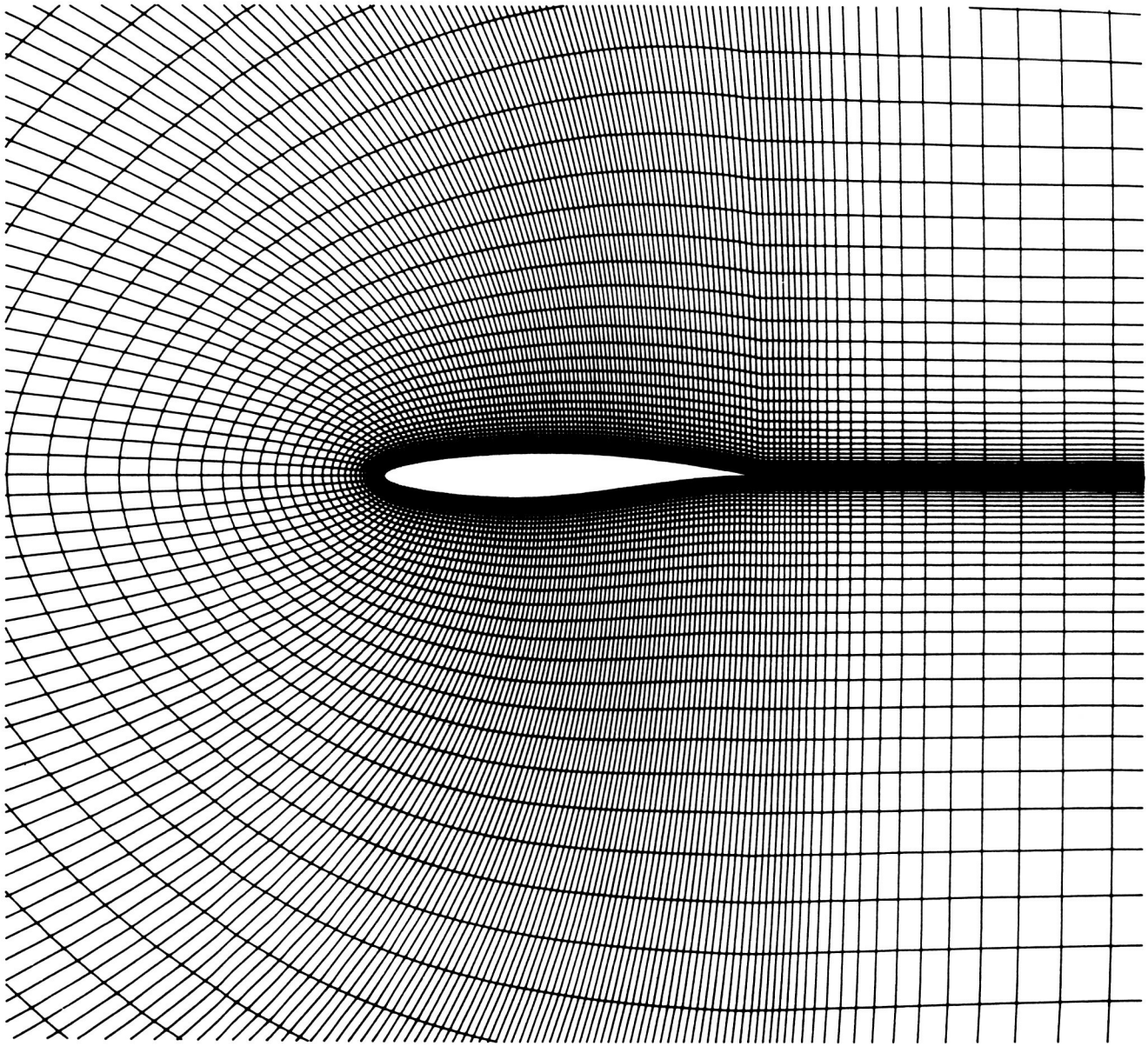

Figure 9a. Partial view of mesh (264 x 100 cells) for RAE 2822 airfoil.

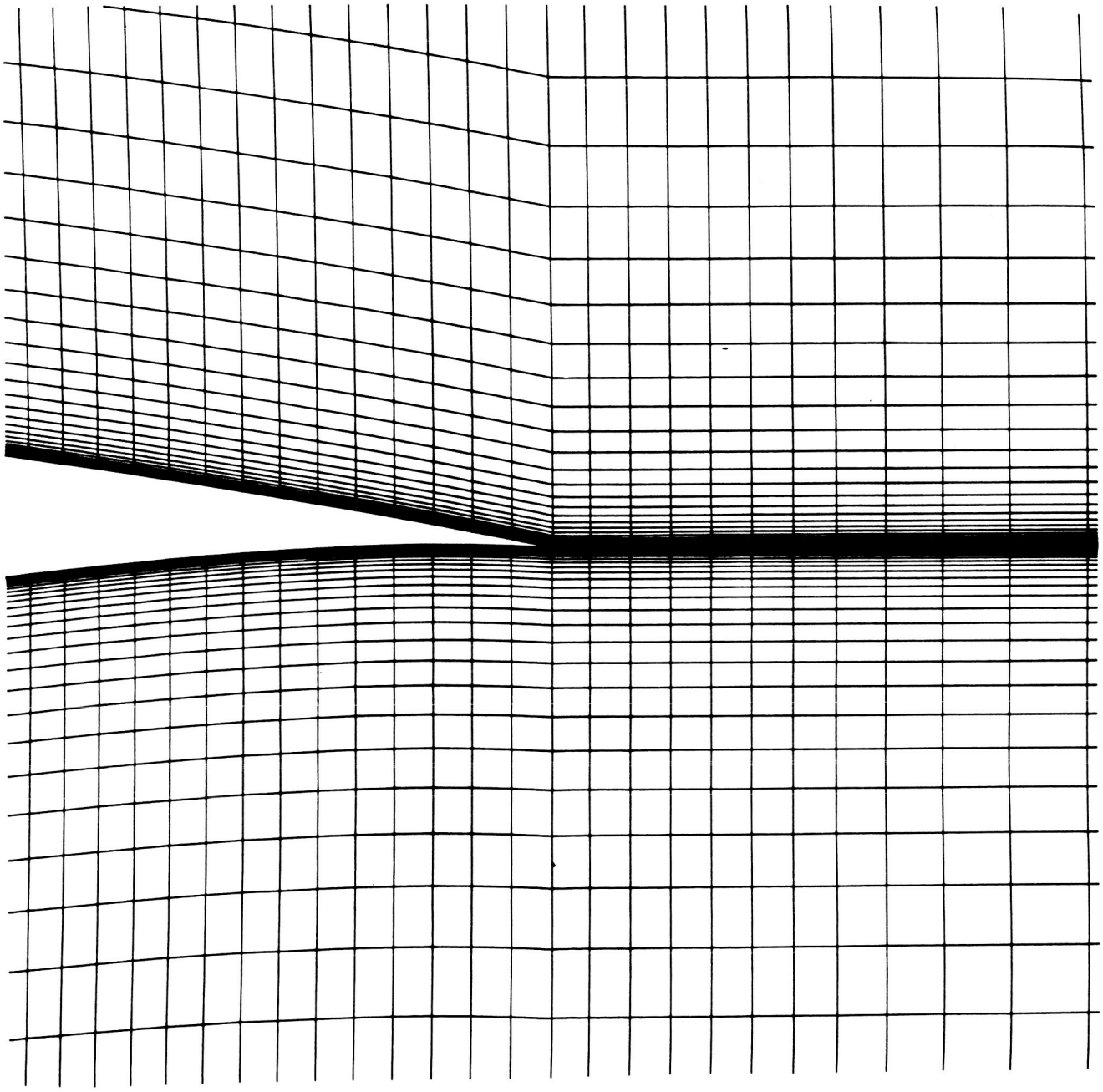

Figure 9b. Blowup of mesh in trailing edge region.

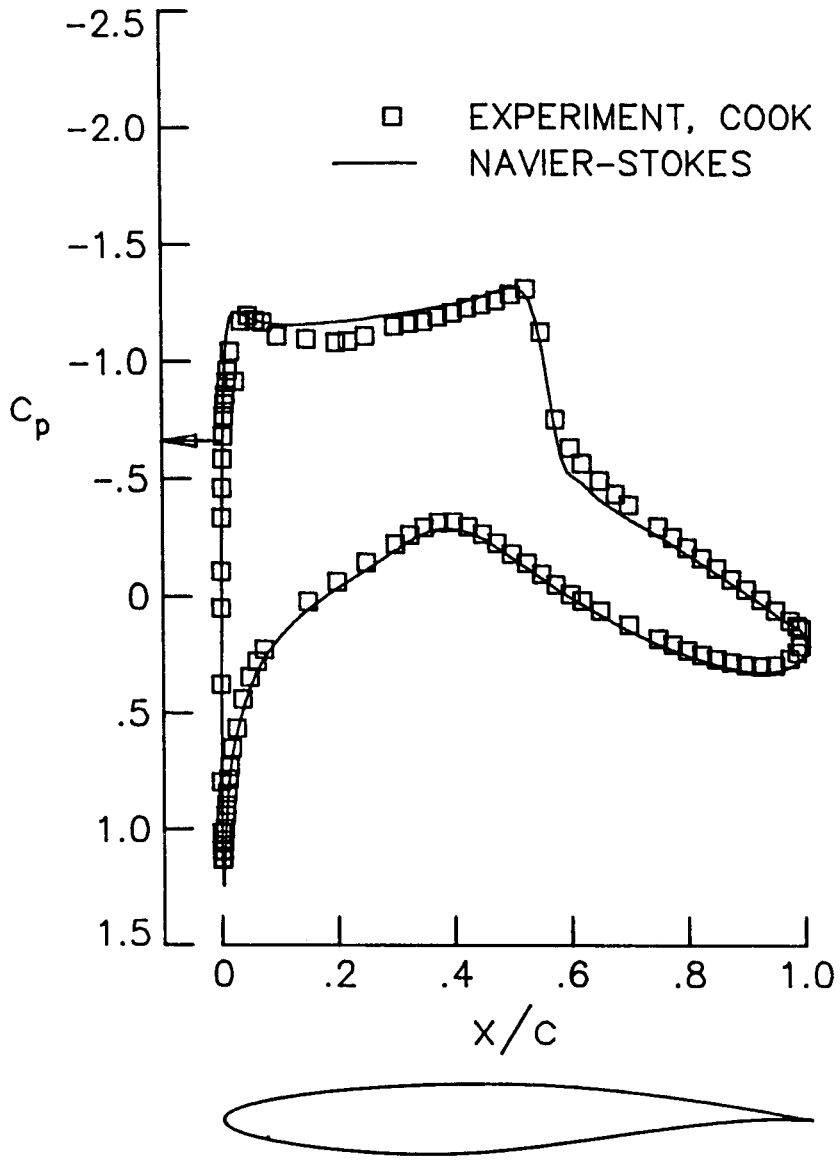

(a) Pressure distribution.

Figure 10. Calculation of turbulent flow over RAE 2822 airfoil with basic artificial dissipation model ($M_\infty = 0.73$, $Re_\infty = 6.5 \times 10^6$, $\alpha = 2.79^\circ$).

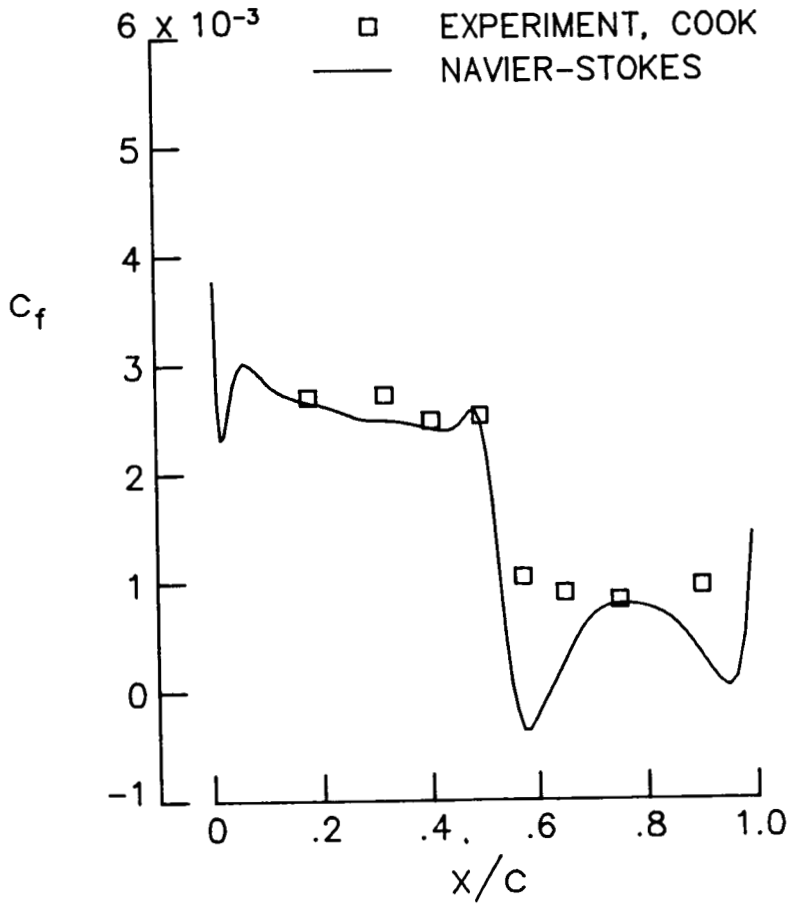

(b) Upper surface skin-friction distribution.

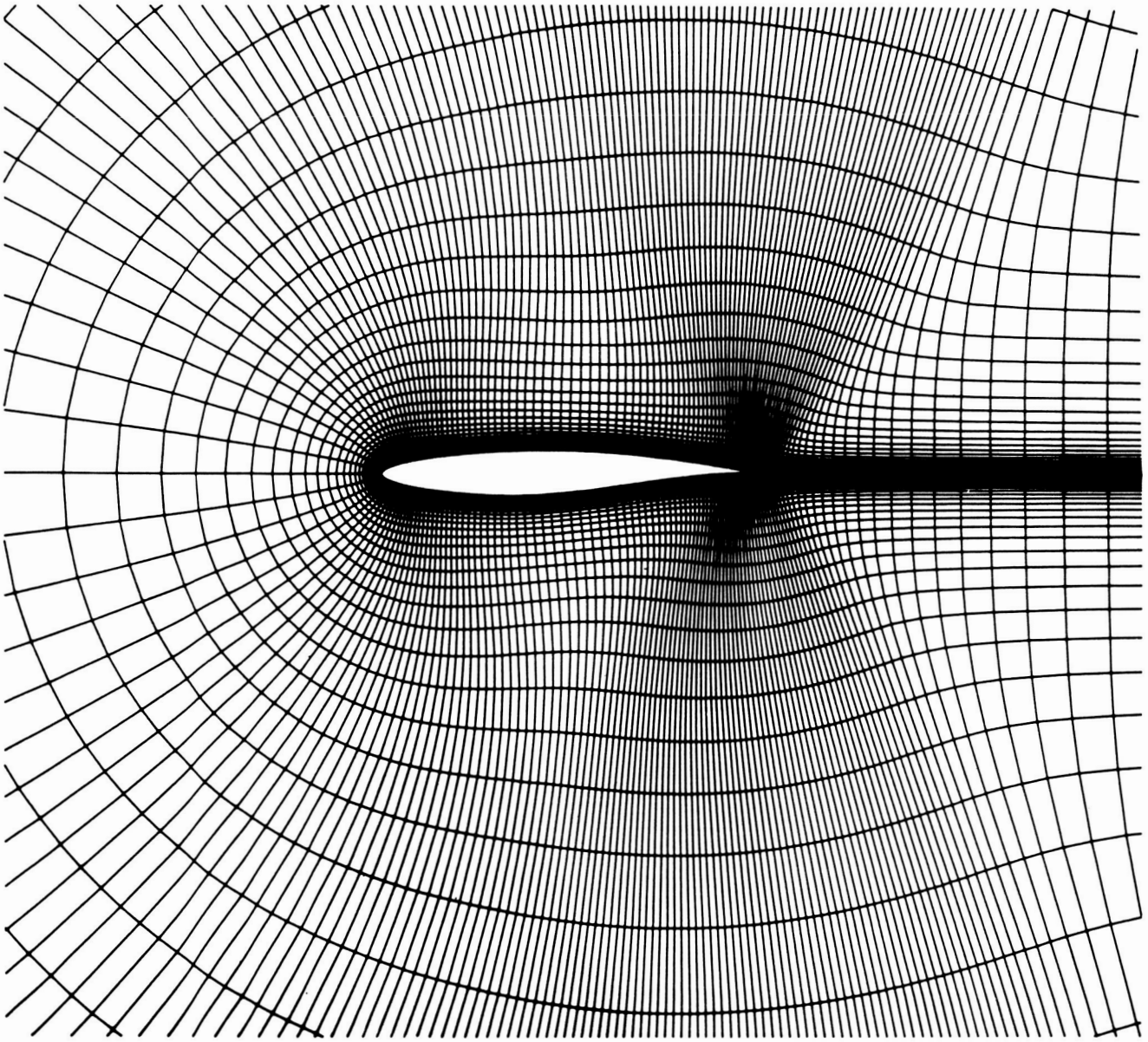

Figure 11a. Partial view of mesh (256 x 64 cells) for RAE 2822 airfoil; mesh refinement at trailing edge.

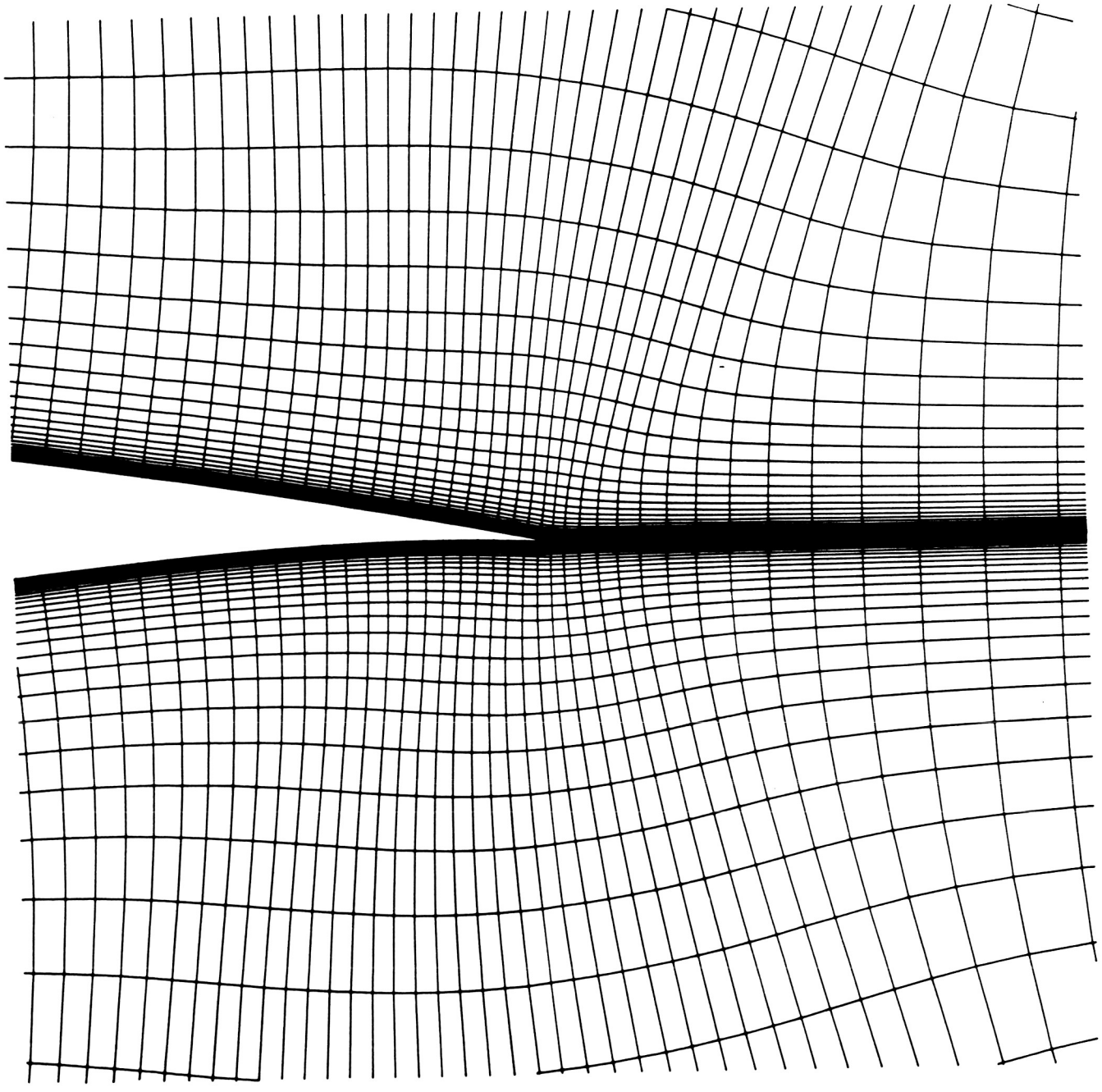

Figure 11b. Blowup of mesh in trailing edge region.

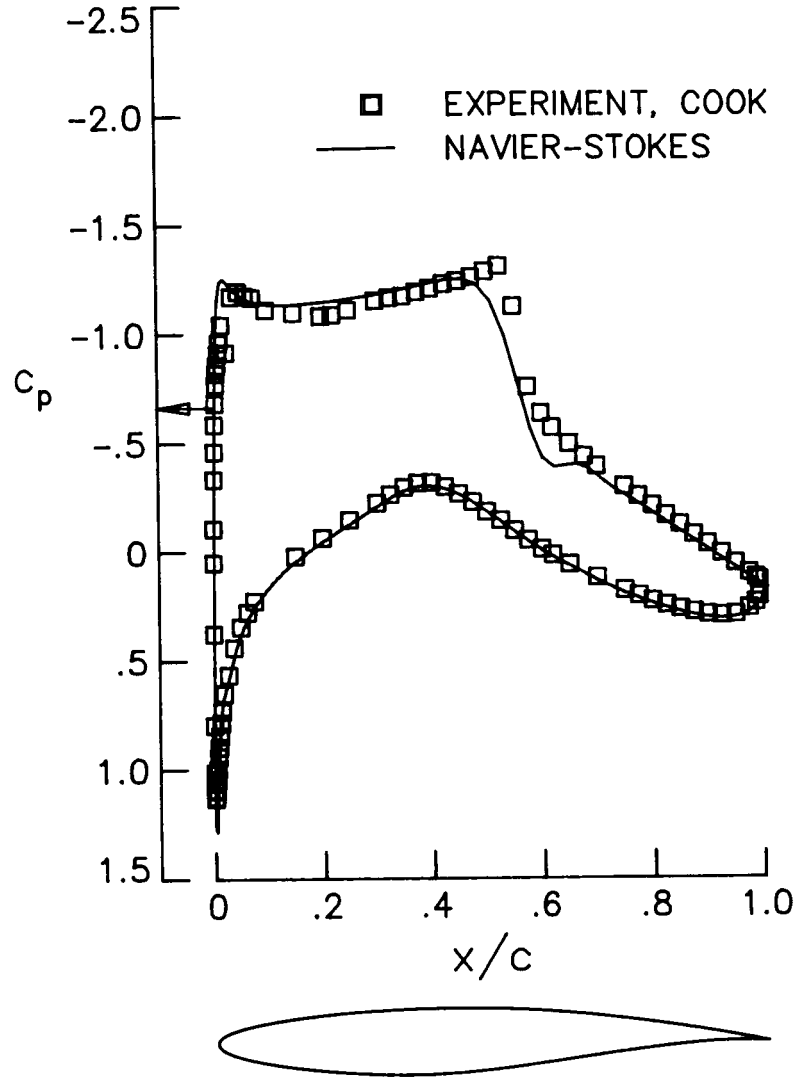

(a) Pressure distribution.

Figure 12. Calculation of turbulent flow over RAE 2822 airfoil with basic artificial dissipation model and mesh refinement at trailing edge (M_∞ = 0.73, Re_∞ = 6.5 x 10^6, α = 2.79°).

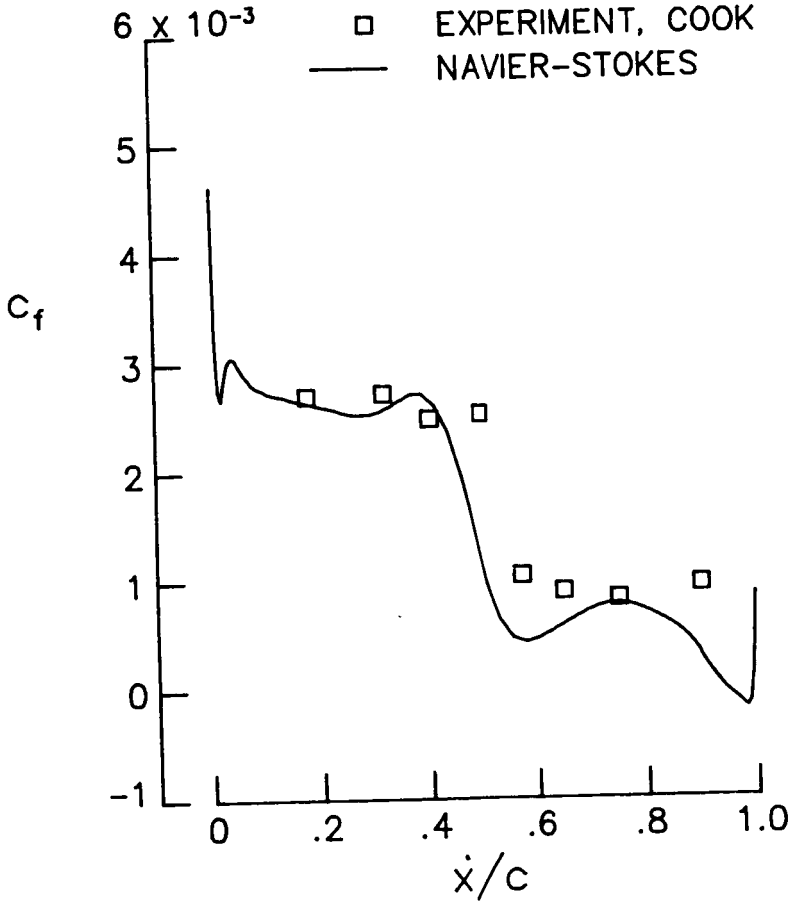

(b) Upper surface skin-friction distribution.

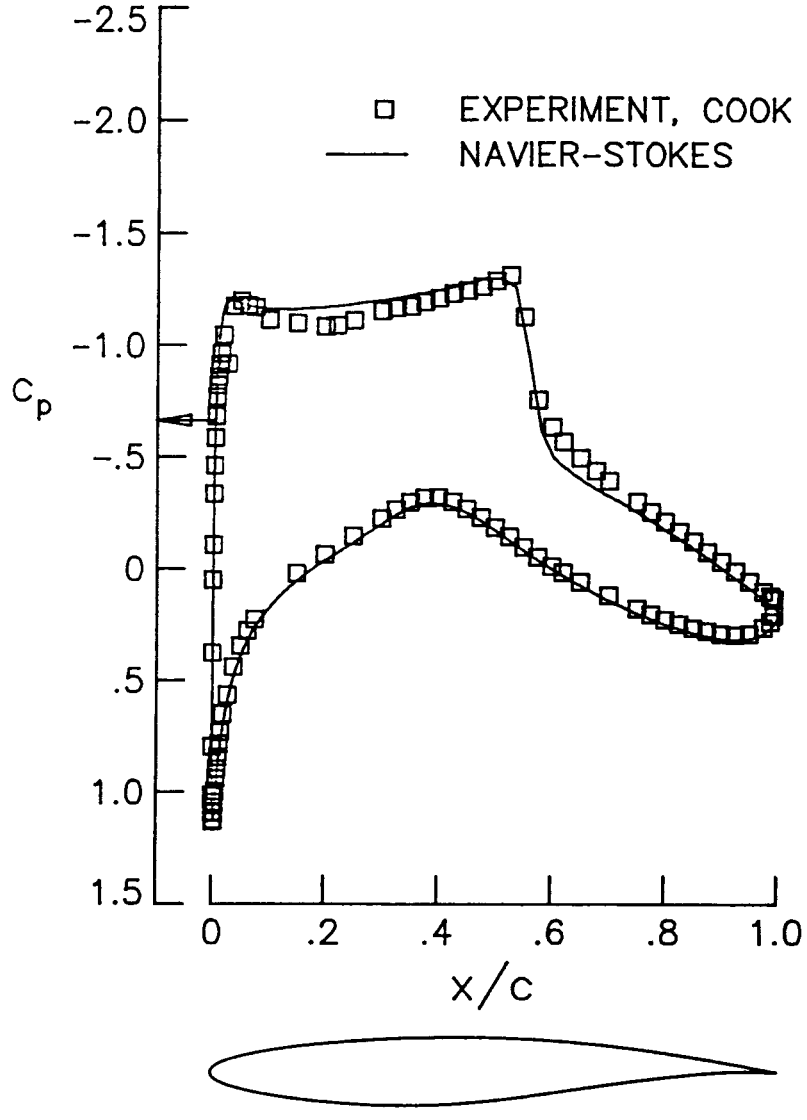

(a) Pressure distribution.

Figure 13. Calculation of turbulent flow over RAE 2822 airfoil with modified (Eq. 16)) artificial dissipation model and mesh refinement at trailing edge ($M_\infty = 0.73$, $Re_\infty = 6.5 \times 10^6$, $\alpha = 2.79^\circ$).

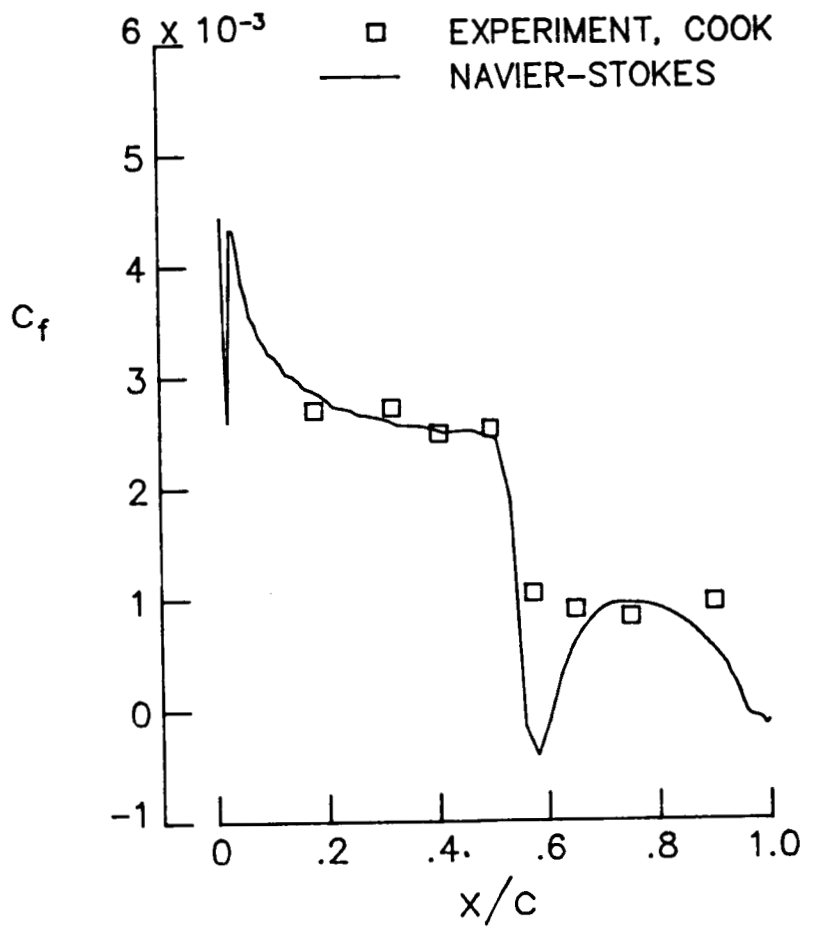

(b) Upper surface skin-friction distribution.

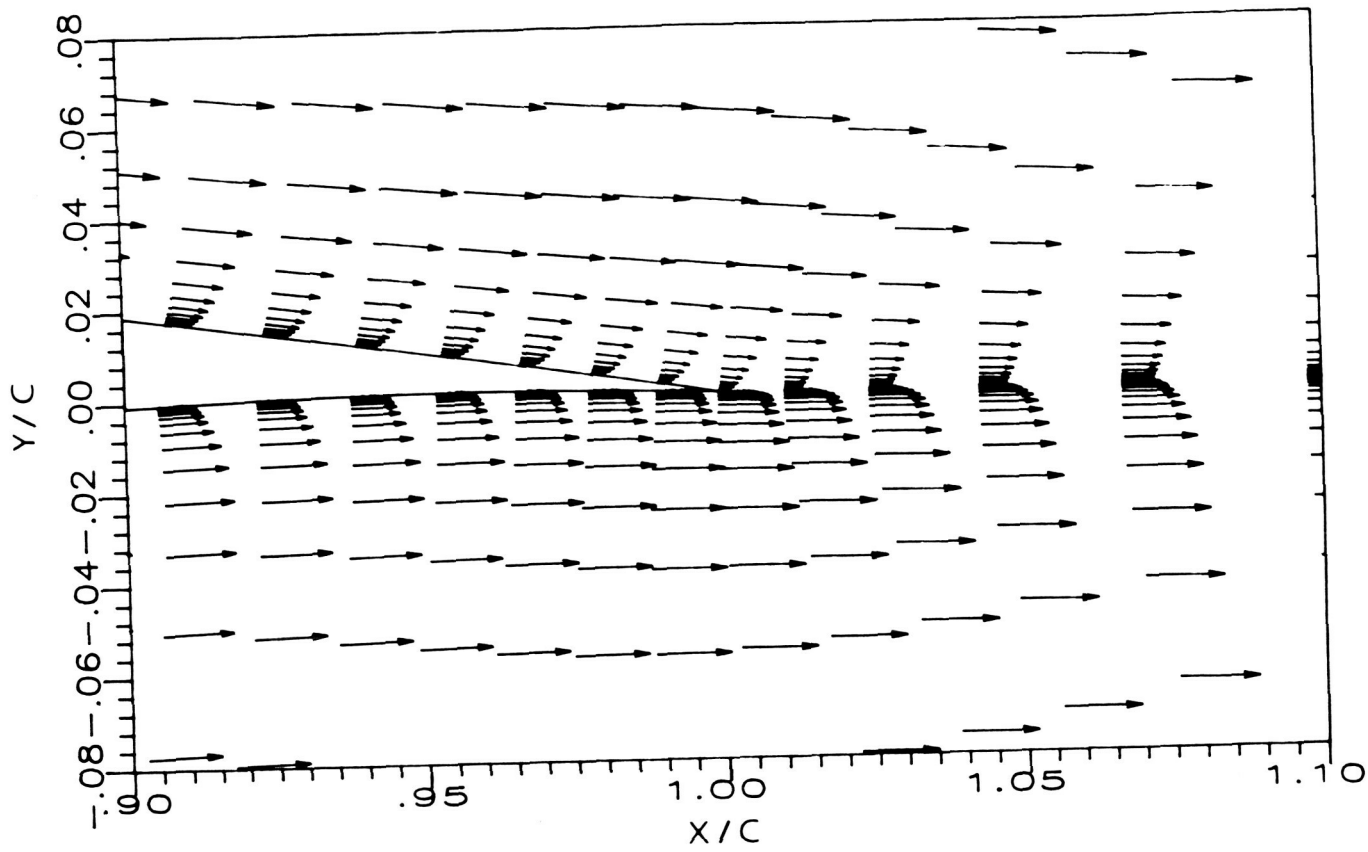

(c) Velocity vectors at trailing edge.

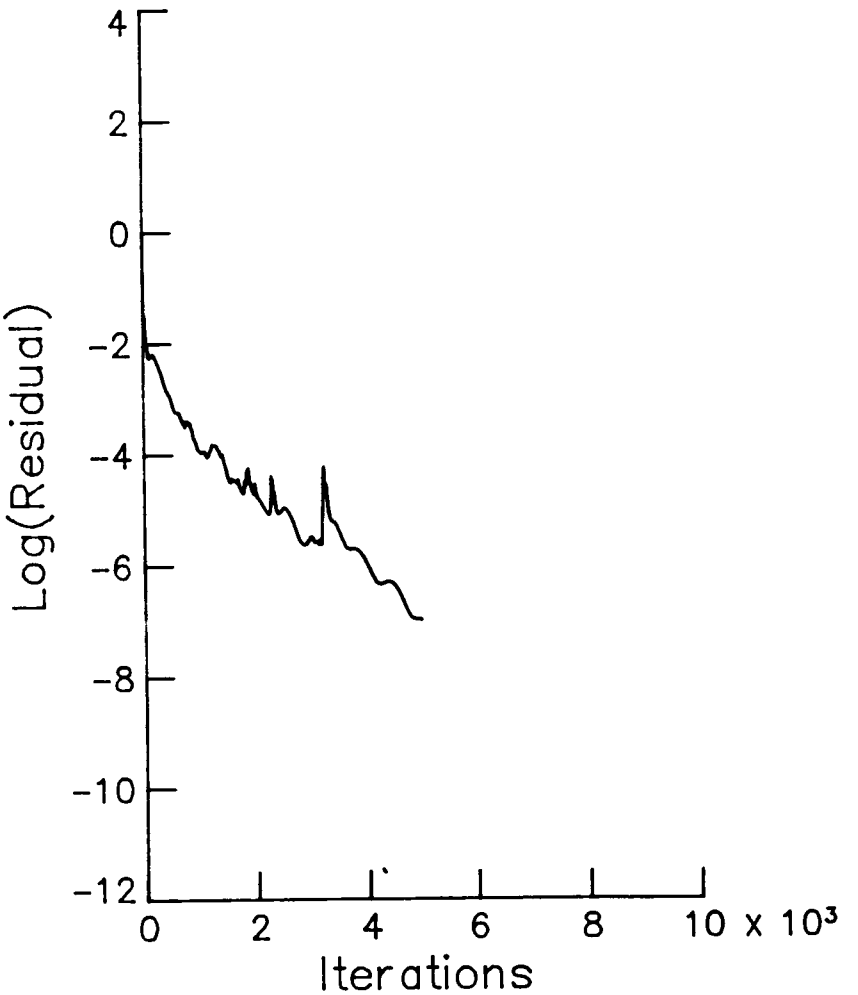

(d) Residual and lift histories (without multigrid).

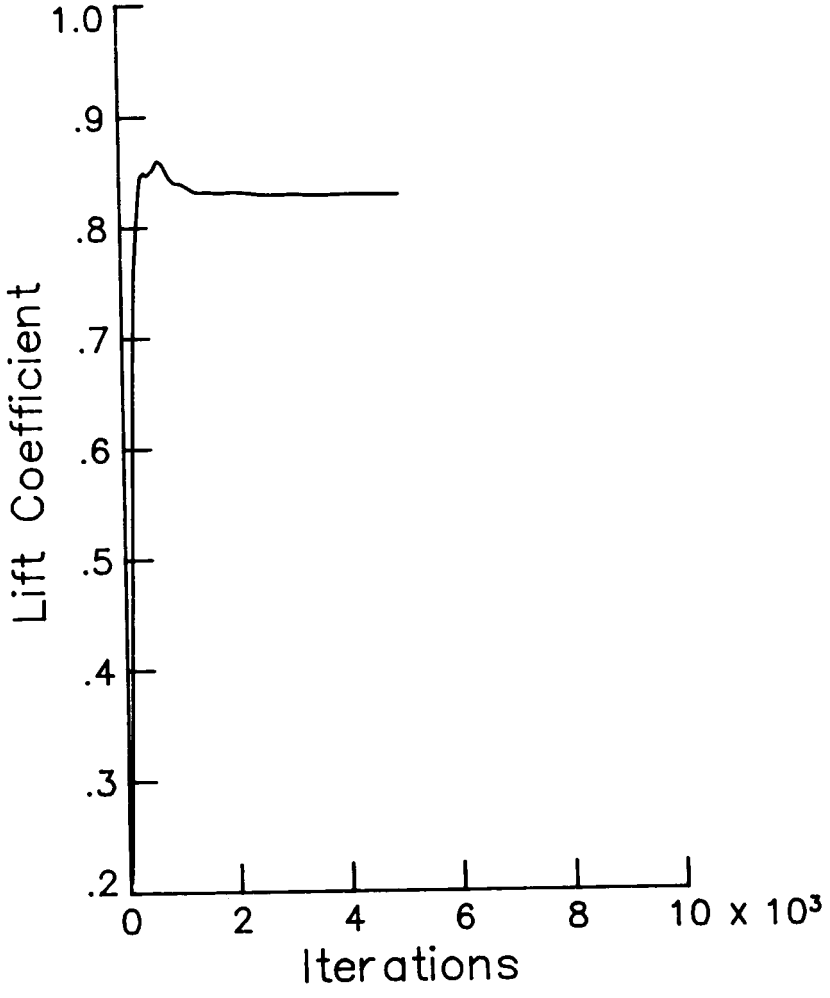

(d) Residual and lift histories (without multigrid).

Standard Bibliographic Page

1. Report No. NASA CR-178296 ICASE Report No. 87-29	2. Government Accession No.	3. Recipient's Catalog No.
4. Title and Subtitle ARTIFICIAL DISSIPATION AND CENTRAL DIFFERENCE SCHEMES FOR THE EULER AND NAVIER-STOKES EQUATIONS		5. Report Date April 1987 6. Performing Organization Code
7. Author(s) R. C. Swanson and Eli Turkel		8. Performing Organization Report No. 87-29
9. Performing Organization Name and Address Institute for Computer Applications in Science and Engineering Mail Stop 132C, NASA Langley Research Center Hampton, VA 23665-5225		10. Work Unit No. 11. Contract or Grant No. NAS1-18107
12. Sponsoring Agency Name and Address National Aeronautics and Space Administration Washington, D.C. 20546		13. Type of Report and Period Covered Contractor Report 14. Sponsoring Agency Code 505-90-21-01

15. Supplementary Notes

Langley Technical Monitor:
J. C. South

Final Report

Submitted to Proc. of the AIAA 8th Computational Fluid Dynamics Conference

16. Abstract

An artificial dissipation model, including boundary treatment, that is employed in many central difference schemes for solving the Euler and Navier-Stokes equations is discussed. Modifications of this model such as the eigenvalue scaling suggested by upwind differencing are examined. Multistage time stepping schemes with and without a multigrid method are used to investigate the effects of changes in the dissipation model on accuracy and convergence. Improved accuracy for inviscid and viscous airfoil flows is obtained with the modified eigenvalue scaling. Slower convergence rates are experienced with the multigrid method using such scaling. The rate of convergence is improved by applying a dissipation scaling function that depends on mesh cell aspect ratio.

17. Key Words (Suggested by Authors(s))	18. Distribution Statement
artificial dissipation	34 - Fluid Mechanics and Heat Transfer 64 - Numerical Analysis Unclassified - unlimited

19. Security Classif.(of this report)	20. Security Classif.(of this page)	21. No. of Pages	22. Price
Unclassified	Unclassified	54	A04

For sale by the National Technical Information Service, Springfield, Virginia 22161